



(2)

**Woods Hole
Oceanographic
Institution**

DTIC
ELECTE
S F D
MAR 07 1994



**A Preliminary Study of Shallow-Water Sonar Issues:
Signal Motion Loss and Reverberation Noise**

by

W. Kenneth Stewart, Dezhang Chu, and Xiaou Tang

"Original contains color
plates: All DTIC reproductions
will be in black and
white"

September 1993

Technical Report

Funding was provided by the Mitre Corporation and the Office of Naval Research
under Contract N00014-92-C-6028

Approved for public release; distribution unlimited.

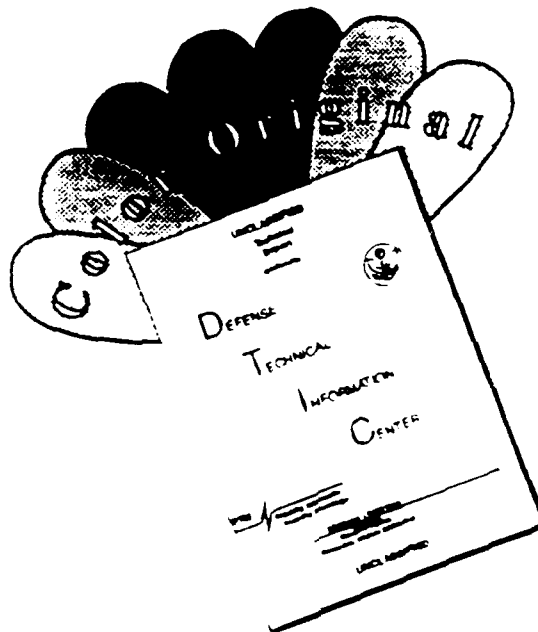
94-07404



DTIC QUALITY INSPECTED 1

94 3 4 073

DISCLAIMER NOTICE



THIS DOCUMENT IS BEST QUALITY AVAILABLE. THE COPY FURNISHED TO DTIC CONTAINED A SIGNIFICANT NUMBER OF COLOR PAGES WHICH DO NOT REPRODUCE LEGIBLY ON BLACK AND WHITE MICROFICHE.

WHOI-93-41

**A Preliminary Study of Shallow-Water Sonar Issues:
Signal Motion Loss and Reverberation Noise**

by

W. Kenneth Stewart, Dezhang Chu, and Xiaou Tang

**Woods Hole Oceanographic Institution
Woods Hole, Massachusetts 02543**

September 1993

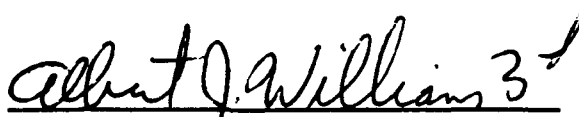
Technical Report

**Funding was provided by the Mitre Corporation and the Office of Naval Research
under Contract N00014-92-C-6028**

**Reproduction in whole or in part is permitted for any purpose of the United States
Government. This report should be cited as Woods Hole Oceanog. Inst. Tech. Rept.,
WHOI-93-41.**

Approved for public release; distribution unlimited.

Approved for Distribution:



**George V. Frisk, Chair
Department of Applied Ocean Physics and Engineering**

Accession For	
NTIS CRA&I	<input checked="checked" type="checkbox"/>
DTIC TAB	<input type="checkbox"/>
Unannounced	<input type="checkbox"/>
Justification	
By	
Distribution /	
Availability Codes	
Dist	Avail and/or Special
A-1	

A Preliminary Study Of Shallow-Water Sonar Issues: Signal Motion Loss and Reverberation Noise

W. Kenneth Stewart, Dezhang Chu, and Xiaoou Tang

**Department of Applied Ocean Physics and Engineering
Woods Hole Oceanographic Institution
Woods Hole, MA 02543**

20 September 1993

Executive Summary

This preliminary investigation addresses key program elements for sonar sensing in a shallow-water environment before development of a full Navy proposal. Such an investigation is fundamental to the establishment of bounds on possible solutions and to the reduction of program uncertainty. The modeling and experimental program addressed here is limited to two issues—the potential degradation of sonar data due to signal masking by shallow-water reverberation and signal loss caused by extreme platform motions. These two issues were selected as a research focus because they are unique to the shallow-water environment and no literature exists to guide project development.

The research program combined theoretical modeling of the two phenomena, experimental validation in a shallow-water environment, and further development of a computer model to explore parametric sensitivity. Models simulating the signal motion loss caused by extreme platform motions were developed. A reverberation model for estimating the average reverberation intensity in the shallow water environment is presented. Computer simulation results show that the performance of the models is good. These results are compared with real sonar data from an initial dock-side test, which shows good agreement with the theoretical prediction.

As a result of the shallow-water experiments and acoustic modeling, we conclude that: (1) Signal motion loss is not the dominant factor for sonars in the frequency range of interest (>200 kHz); rather, a high-quality (velocity-aided) inertial navigation and attitude system will be sufficient to correct for geometric distortions caused by platform motion. (2) Although surface reverberation and multipath noise can be a factor, particularly in shadow-mode imaging, reverberation levels are rapidly attenuated at the frequencies of interest and beam patterns can be manipulated to reject most interferences; echo-mode imaging is still dominated by the contrast between target strength and bottom reverberation.

1.0 INTRODUCTION

It is anticipated that future wars will involve third-world scenarios characterized by special operations/low-intensity conflicts (SOLIC) with amphibious assaults such as that used in the Persian Gulf war. Doctrine calls for both ingress and egress assault lanes, each approximately 150-m wide and up to 2-km long for a regimental-sized assault force. Current above-water detonation technology, which seeks to explode mines with significant overpressure, has been shown to be minimally effective. As a result, it is expected that there will be up to 50 mines in areas of depth less than 10 ft, which will be cleared using such direct-contact techniques as towed sleds. There will also be approximately 10 to 15 mines in the shallow-water area between 10 and 80 ft of depth. These mines will consist of both older metal-based, contact technology and newer composite-based influence mines ranging in size from 3-ft diameter in the deeper water to 6-in diameter near the surf zone. The mines can be triggered from sensed magnetic or electromagnetic fields, sound, overpressure, or contact.

Special-warfare personnel are currently deployed to emplace detonators on shallow-water mines for subsequent destruction. The deployment and recovery of these swimmers is extremely dangerous because of premature detonations, malfunctioning equipment, and enemy defenders. MITRE's Autonomous Systems Laboratory (ASL) and the Deep Submergence Laboratory (DSL) of the Woods Hole Oceanographic Institution (WHOI) have been working with the Navy to develop a proposal for the demonstration of small underwater vehicles, supervised by humans operators remote from the hazardous operation, to clear mines in the shallow-water area. We believe that such semi-autonomous underwater vehicles (SAUVs) can be an effective asset for shallow-water mine countermeasures when designed and equipped with appropriate sensors and actuators, all under the high-level management of recently developed AI techniques for situated reasoning.

2.0 APPROACH

In considering a long-term approach to the problems of mine countermeasures in a shallow-water environment by an SAUV, we generally partition our approach into three components: remote sensing and machine perception; platform engineering and closed-loop control; and reactive tactical control and mission management. For each component, we have focused two key experiments as a means of addressing major programmatic uncertainties. The results of these experiments will be used as initial parameters for a system-level simulation of the larger problem.

A full treatment of the problem is not addressed here. Instead, we focus on sensing issues germane to any solution for detection, classification, and task-relative servoing, whether accomplished manually or semi-autonomously. Successful completion of such mission components will be largely determined by the quality of available sonar data. The two environmental effects expected to most significantly degrade such data are signal masking by shallow-water reverberation and signal loss caused by extreme platform motions. To address these two issues our research program combined theoretical modeling, experimental validation in a shallow-water environment, and further development of a computer model to explore parametric sensitivity.

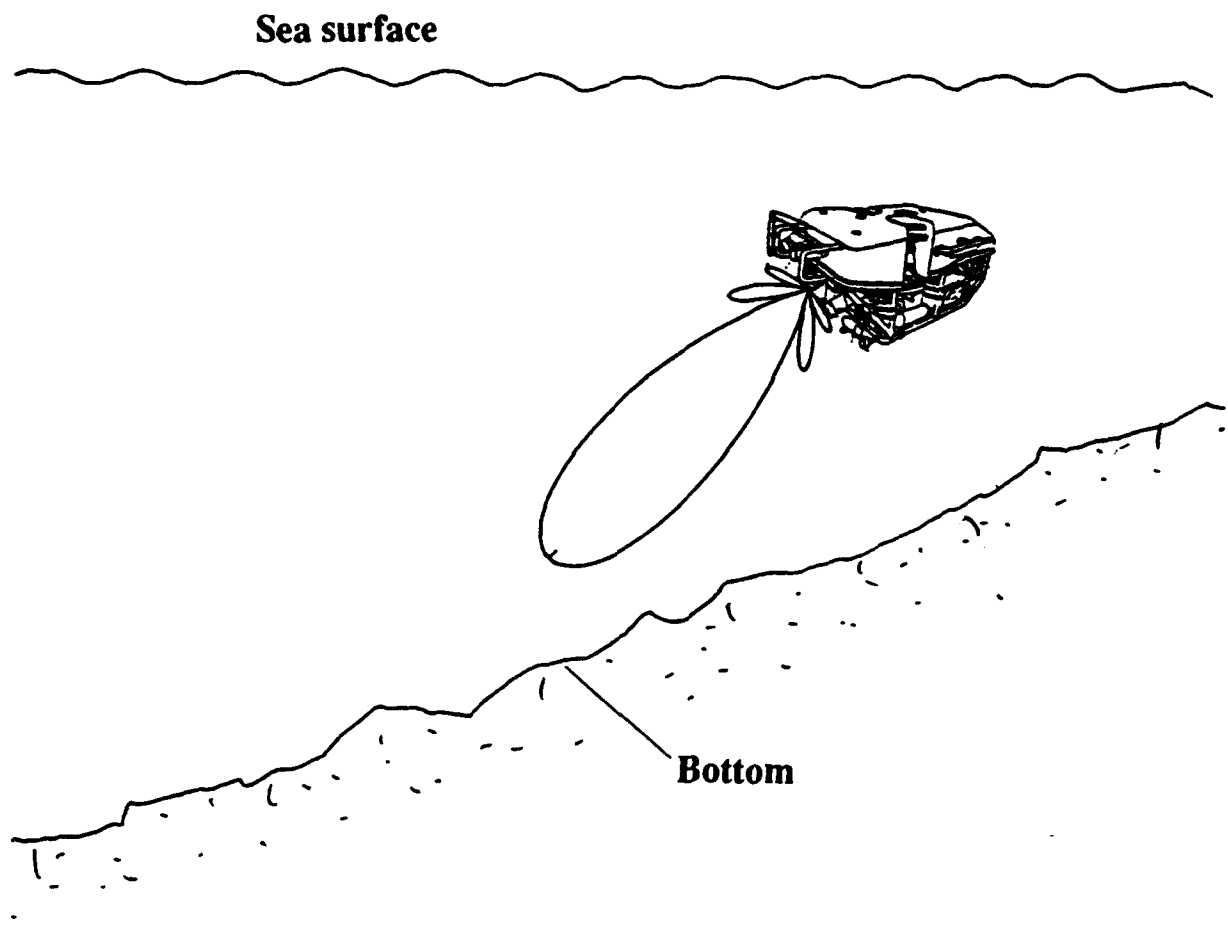


Figure 1 Geometry of shallow-water experiments off WHOI dock, showing a 300-kHz forward-scan sonar mounted on a remotely-operated vehicle.

2.1 Shallow-Water Experiments

To support theoretical analysis and numerical modeling, experimental testing was conducted in a shallow-water environment off the WHOI dock using a remotely operated vehicle (ROV). Figure 1 depicts the (down-looking) geometry for the experiments, which used a 300-kHz forward-scan sonar, mechanically rotated with a precision stepping motor (Fig. 2). Although the ROV was also equipped with a 200-kHz sidescan sonar, tight scheduling constraints limited the amount of time available for testing, and efforts focused on the 300-kHz system. This was not a severe drawback because the sonar's narrow horizontal beams are identical to a typical sidescan system and could be used to validate both side- and forward-look geometries.

The forward-scan sonar is a member of DSL's family of phase-difference systems, which includes 120-kHz, 200-kHz, and 300-kHz sonars designed for seafloor imaging and swath-bathymetric mapping. The sonars were developed by DSL in conjunction with the Applied Physics Laboratory (APL) of the University of Washington and Acoustic Marine Systems, Inc. of Redmond, Washington.

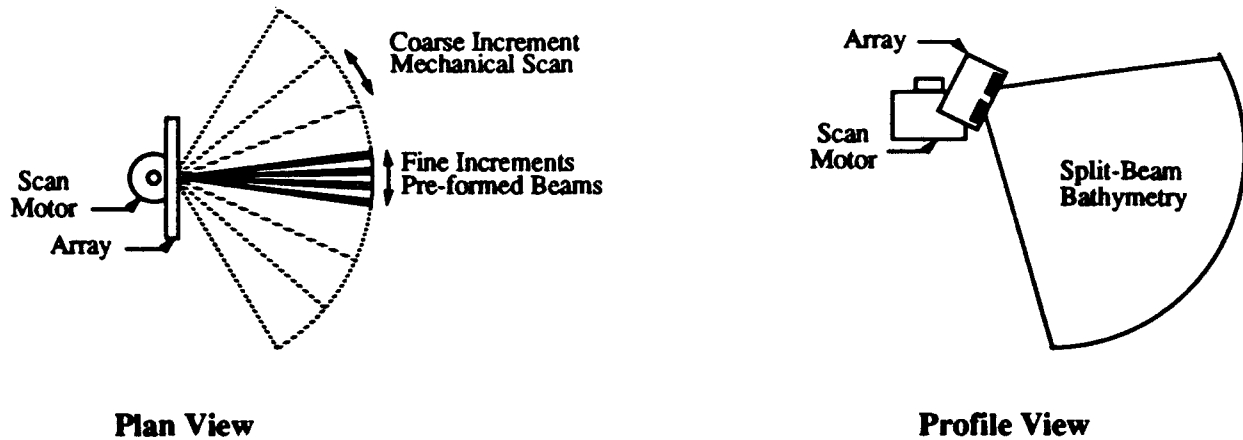


Figure 2 300-kHz scanning-sonar geometry.

The system has been fully characterized against reference hydrophones at the APL acoustic calibration facility to quantify source level, beam pattern, receiver sensitivity, and system gain; both near- and far-field responses were considered. The dual-receiver design also provides phase information that can be used to generate high-resolution swath bathymetry; system calibration includes phase-center separation and acoustic-axis offset.

Transmit state, repetition rate, pulse length, and gain of the systems are operator selectable. Other significant features include digitization at the receiver, multiple channels of quadrature-detected data, and a high-bandwidth optical-fiber link to the surface. For each receiver channel (two per beam), a surface-selectable step gain is applied and the antialiased signal is quadrature sampled at 10 kHz. The digital signal is Manchester encoded at a 2-MHz clock rate and transmitted to the surface over a fiber-optic serial link (eight 16-bit numbers per sampling interval). At the surface, the serial stream is decoded and digital data are transferred to the surface processor and merged with navigation (pressure depth, acoustic x-y-z) and attitude (flux-gate compass, gyro, pitch, roll) data, then time stamped and recorded in digital form on 8-mm helical-scan tape.

3.0 SIGNAL MOTION LOSS (SML)

3.1 Background

A sidescan sonar signal is generally displayed and evaluated as a backscattered-intensity image. For such images, there are two primary types of distortion, geometric and radiometric (intensity). The former corresponds to a discrepancy between the relative location of the feature on the image and its true location on the seafloor; the latter is a deviation from the ideal linear relation between image intensity and backscattering strength of the materials on the seafloor. Various kinds of distortions can be identified in each of these two categories [1], [2].

Intensity distortions in sidescan sonar images arise from a number of different sources. Spherical spreading and attenuation in water cause the acoustical intensity to decrease as sound

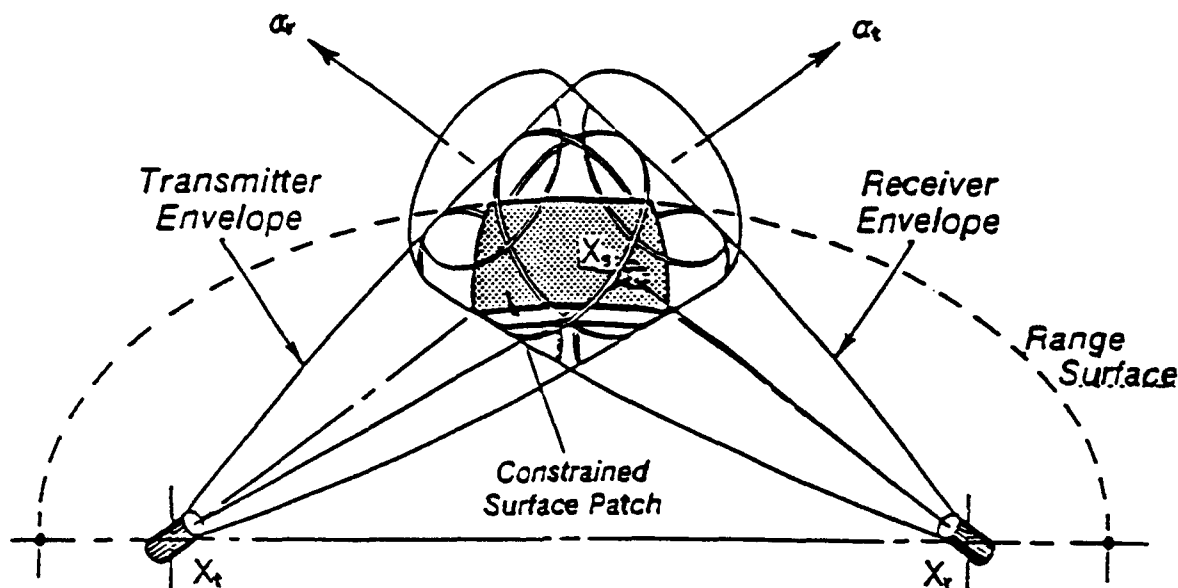


Figure 3 Geometry of transmission and reception for a backscattered acoustic signal. The more general bistatic case encompasses monostatic operation.

propagates away from the vehicle. Another factor that affects the signal power is the decrease in backscattering intensity due to diminishing grazing angles at increasingly longer range. Extensive research has been carried out to mitigate the problems associated with such distortions [1]-[6]. The general approach is to apply a time-varying gain (TVG) to the returned signal, allowing the user to adjust the image intensity to make it as uniform as possible.

However, another intensity distortion, which corresponds to the platform motion of a vehicle, remains almost untouched by previous work. The platform motion could cause unexpected and unpredictable misalignment of the transmitting and receiving beam patterns, resulting in a drop in the power level of the returned signal. Previous investigations have not addressed this problem for three reasons: (a) the lack of precise navigation information makes it hard to evaluate the significance of the problem, (b) the traditional use of sidescan sonar in calmer deep water makes it less significant than in a shallow-water environment, and (c) the broader azimuth beam width (at typically lower frequencies) makes the received signal level relatively insensitive to platform motion.

3.2 Theoretical Model

Figure 3 [1] illustrates the geometry of motion-loss distortion. At time t_0 , the transmitter, at position x_t , emits a pulse of acoustic energy in the direction $\alpha(\theta, \phi)$, where θ is the vertical angle and ϕ is the azimuth angle. A receiver with translational and rotational components of motion receives the backscattered acoustic energy. This process is continuous, starting with the transmission of the sonar pulse until it reaches its maximum detectable range. At a time t_1 , the sound scattered by a surface patch x_s reaches the transducer located at the position x_r , which

points in the direction α_r . To describe the motion loss, a signal-motion-loss (SML) coefficient can be defined as:

$$SML(t) = \frac{\int_{x_s} \int B_t(\theta, \phi) B_r(\theta, \phi, t) BSM(\theta, \phi, t) ds}{\int_{x_s} \int B_t^2(\theta, \phi) BSM(\theta, \phi, t) ds} \quad (1)$$

where $B_t(\theta, \phi)$ and $B_r(\theta, \phi)$ are the transmitting and receiving beam patterns, and x_s is the scattering patch on the range-surface ellipse. The backscattering-strength map (BSM) specifies the backscattering intensity on the patch.

In general, the platform has six degrees of freedom, three translational and three rotational. However, we can show that the SML caused by translational motion is small enough to be neglected. Figure 4 compares the misalignment of the beam patterns due to translational motion with that due to rotational motion. Figure 4a shows the effects of a translational motion at 10 m/s, which is much higher than normal vehicle operating speeds. However, the misalignment in beam patterns can hardly be seen due to the considerably higher sound speed (1500 m/s, about two orders of magnitude greater than the vehicle speed).

The scenario is quite different for the rotational case, as shown in Fig. 4b, which corresponds to a rotational speed 10 deg/s. The percentage of the misaligned part increases with time, assuming a constant rotational speed. Although the model developed here includes the translational motion case, calculations show that the SML due to the cross-track translational motion loss is less than 1% and the along-track translational motion at typical vehicle speeds causes only a 5% drop in signal levels. In the following discussion we therefore neglect the motion loss due to the translational motion and consider only the rotational case.

3.2.1 One-Dimensional Model

We begin with the simplest case: a one-dimensional deterministic motion in a homogenous medium. The theoretical beam pattern of a line array is

$$B(\theta) = \left[\frac{\sin\left(\frac{\pi L}{\lambda} \sin(\theta)\right)}{\frac{\pi L}{\lambda} \sin(\theta)} \right]^2, \quad (2)$$

where L is the array length and λ is acoustic wavelength. Figures 5a and 5c show the beam patterns in polar coordinates with rotational speeds of 10 deg/s and 20 deg/s respectively; Figs. 5b and 5d show their counterparts in Cartesian coordinates.

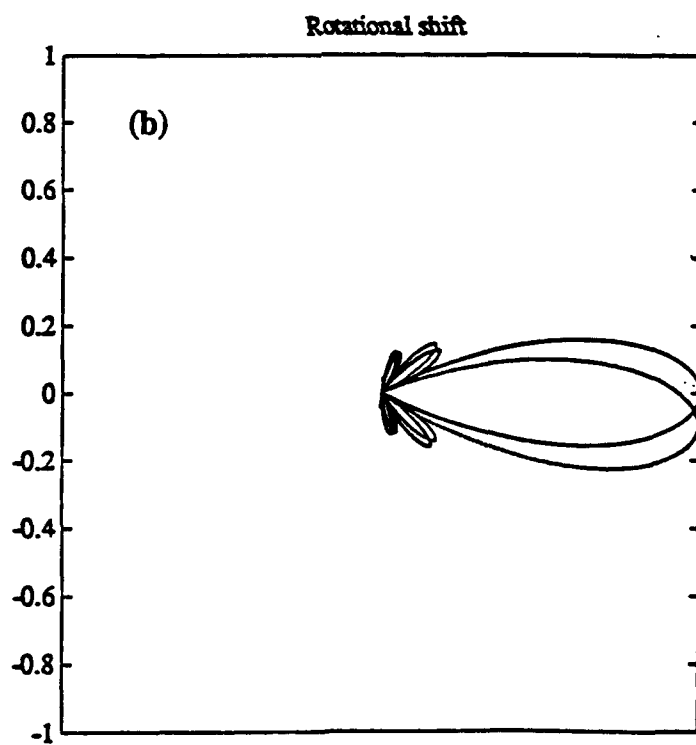
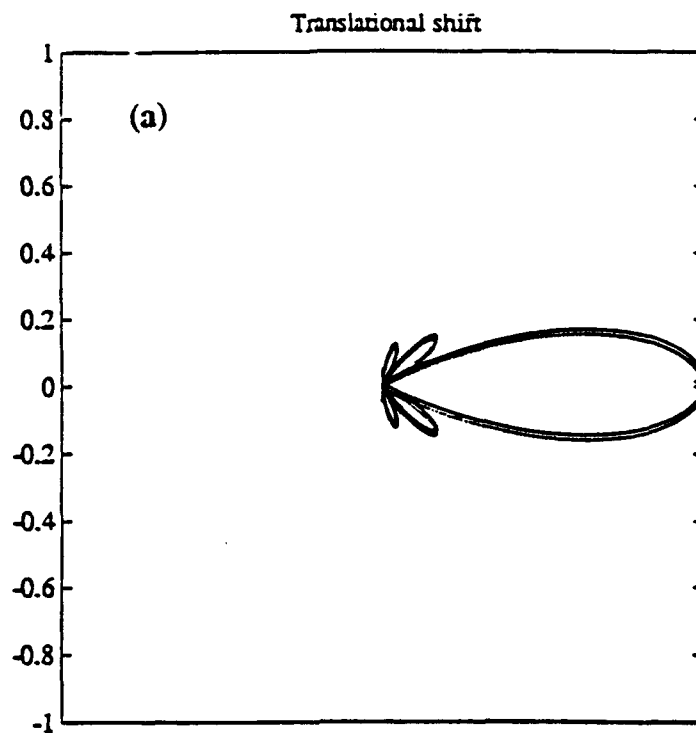
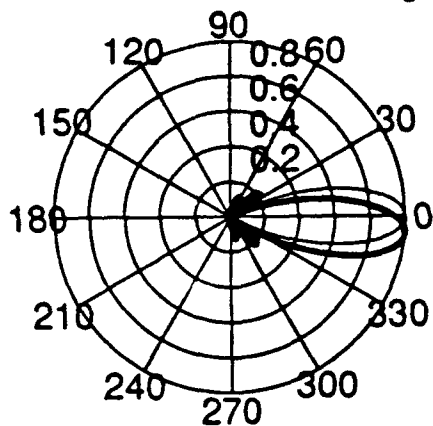


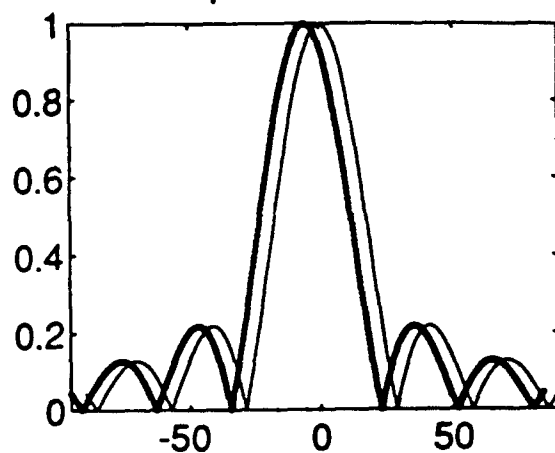
Figure 4 Shifted beam patterns caused by translational and angular platform motions.

Transmit and rotated receiving beams

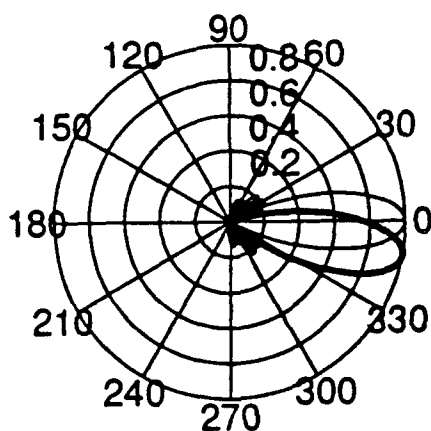


(a)

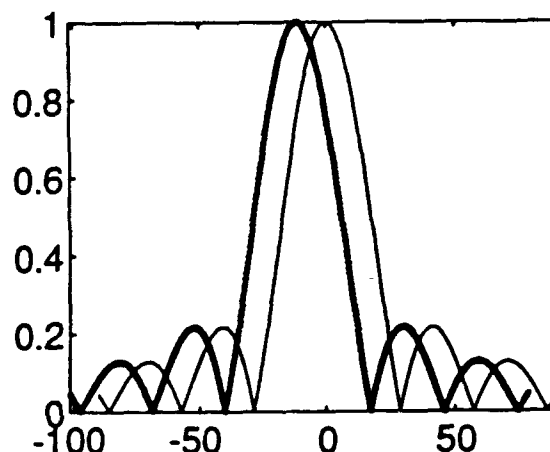
Convolution process of beam rotation



(b)



(c)



(d)

Figure 5 Shifted beam patterns from angular motion in polar (a,c) and cartesian coordinates (b,d). Angular velocities are 10 deg/s (a,b) and 20 deg/s (c,d).

A change in the angle causes the receiver beam pattern to move along the axis. The SML is determined from the integral of the overlapped area. The one-dimensional form of (1) is derived by omitting a proportionality constant [7], giving

$$SML(u) = \int_{-\frac{\pi}{2}}^{\frac{\pi}{2}} B_t(\theta) B_r(u - \theta) d\theta, \quad (3)$$

where u is the angular shift due to platform motion. The uniform medium assumption implies BSM is constant and for our purposes can be assumed to be unity without loss of generality. From

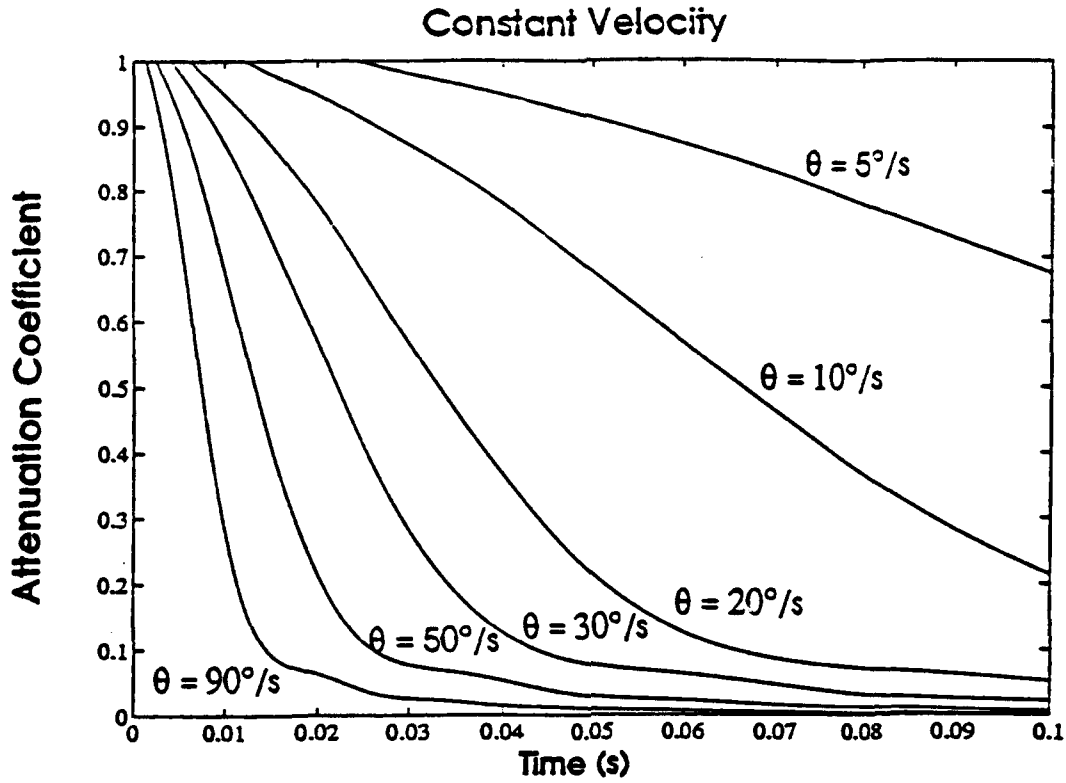


Figure 6 One-dimensional signal motion loss (SML) for constant angular velocity.

Fig. 5 and (3) we see that this is a convolution process. With simplifying assumptions we derive the analytical expression of (3),

$$SML(u) = \frac{1}{2k^4 u^2} \left(\frac{4(\pi - u)}{\pi(2u - \pi)} [\cos((k\pi - ku) - \cos ku)]^2 + 2k\pi \right. \\ \left. - \frac{\pi}{u} \sin(2ku) + \frac{1}{u} (\cos 2ku + 2) \ln\left(\frac{\pi}{\pi - 2u}\right) \right) \quad (4)$$

Figure 6 shows the results of SML computed from (4) as functions of time and rotational speed using a constant speed for each curve, illustrating a descending trend of SML with increasing rotational speed.

3.2.2 Three-Dimensional Model

For a three-dimensional problem, difficulties in analytically taking the double integral of (1) lead us to adopt a numerical approach. Figure 7 shows the 3-D representations of theoretical beam patterns assuming a rectangular array [4],

$$B(\theta, \phi) = \left\{ \text{sinc}\left(\frac{\pi L_x}{\lambda} \sin \theta \cos \phi\right) \text{sinc}\left(\frac{\pi L_y}{\lambda} \sin \theta \sin \phi\right) \right\}^2 \quad (5)$$

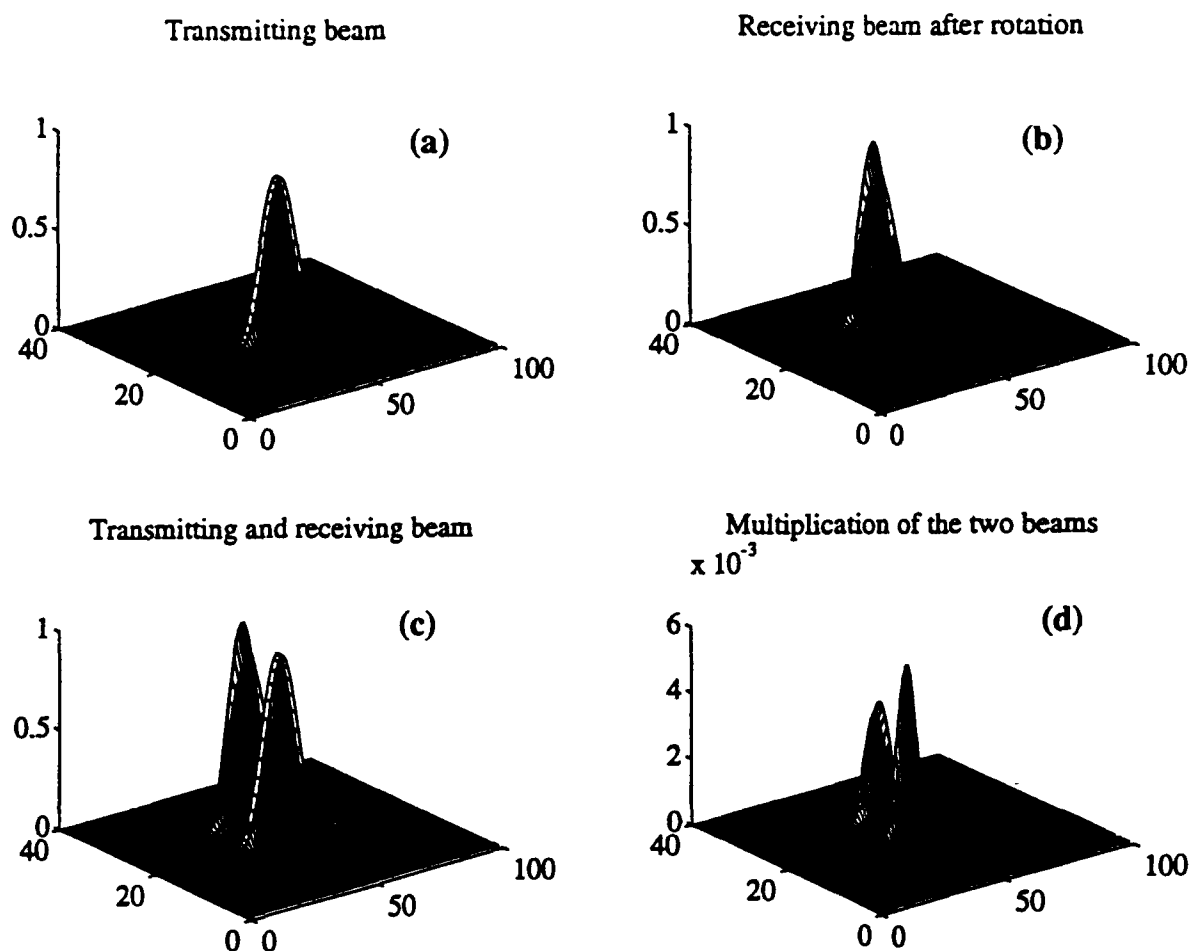


Figure 7 Theoretical transmit and receive beam patterns for a rectangular array.

where L_x and L_y are linear dimensions of the array and $\text{sinc}(x) = \sin(x)/x$. The rotated receiver beam pattern B_r can be calculated by rotating the beam axis using three rotation matrices. Figures 7a and 7b are the transmitting and receiving beam patterns as indicated; Fig. 7c shows the two beam patterns on the same graph. Figure 7d shows the result of multiplying the two beam patterns of Figs. 7a and 7b.

The three angles can be measured relative to the x , y , and z axes (Eulerian) or be expressed as pitch, roll, and yaw, depending upon angular sensor input. At each instant, the vehicle has a yaw rotation speed W_z and a pitch rotation speed W_x . The total effect causes the vehicle to rotate around an axis in the cross-track plane at speed W , where $W^2 = W_x^2 + W_z^2$. The axis can be found as shown in Fig. 8. We rotate the 3-D receiving beam pattern around this axis to get $B_r(\theta, \phi, t)$.

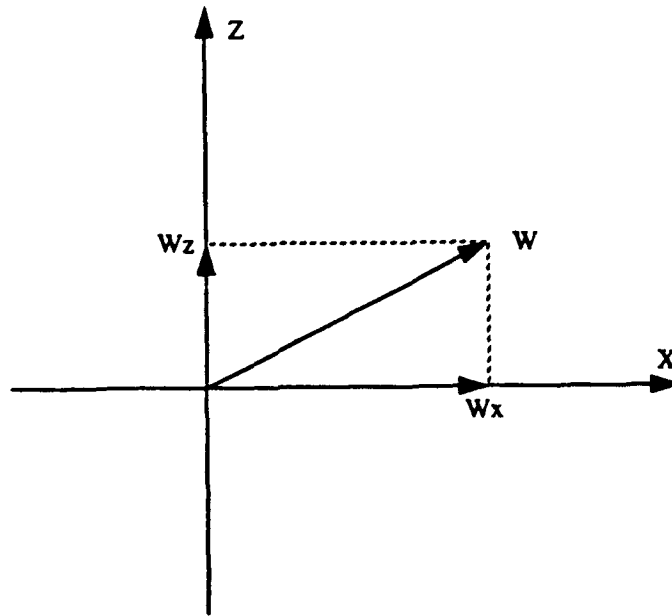


Figure 8 Composition of platform angular velocity.

By taking advantage of the narrower along-track beam of sidescan sonar, we can simplify the problem to two dimensions. The scattering field on the ensonified patch can now be approximated as a constant, allowing us to factor out the BSM function from the integral over ϕ and define a new variable, the vertical-motion-loss coefficient, as

$$VMLC(t, \theta) = \frac{\int B_t(\theta, \phi) B_r(\theta, \phi, t) d\phi}{\int B_t^2(\theta, \phi) d\phi} \quad (6)$$

The advantage of such a definition over (1) is that (6) gives pure motion effects on the scattering field.

Figures 9-11 show computed VMLC using (6). The roll effect is simply a shift of VMLC in θ and is not presented here. Figure 9 shows that the signal loss due to pitch is minimum along the beam axis; Fig. 10 shows that signal loss due to yaw is maximum along beam axis. Figure 11 shows the composition of the two motions giving rise to a shifted motion-loss pattern.

In practice, it is very difficult to measure the angle of rotation at each instant in time corresponding to the sampling interval. Instead we can measure the rotational speed when the sound pulse is transmitted then approximate the motion as linear with a constant speed. We can make this assumption because of the short pulse length of a high-frequency sonar and a relatively

MOTION LOSS COEFFICIENT

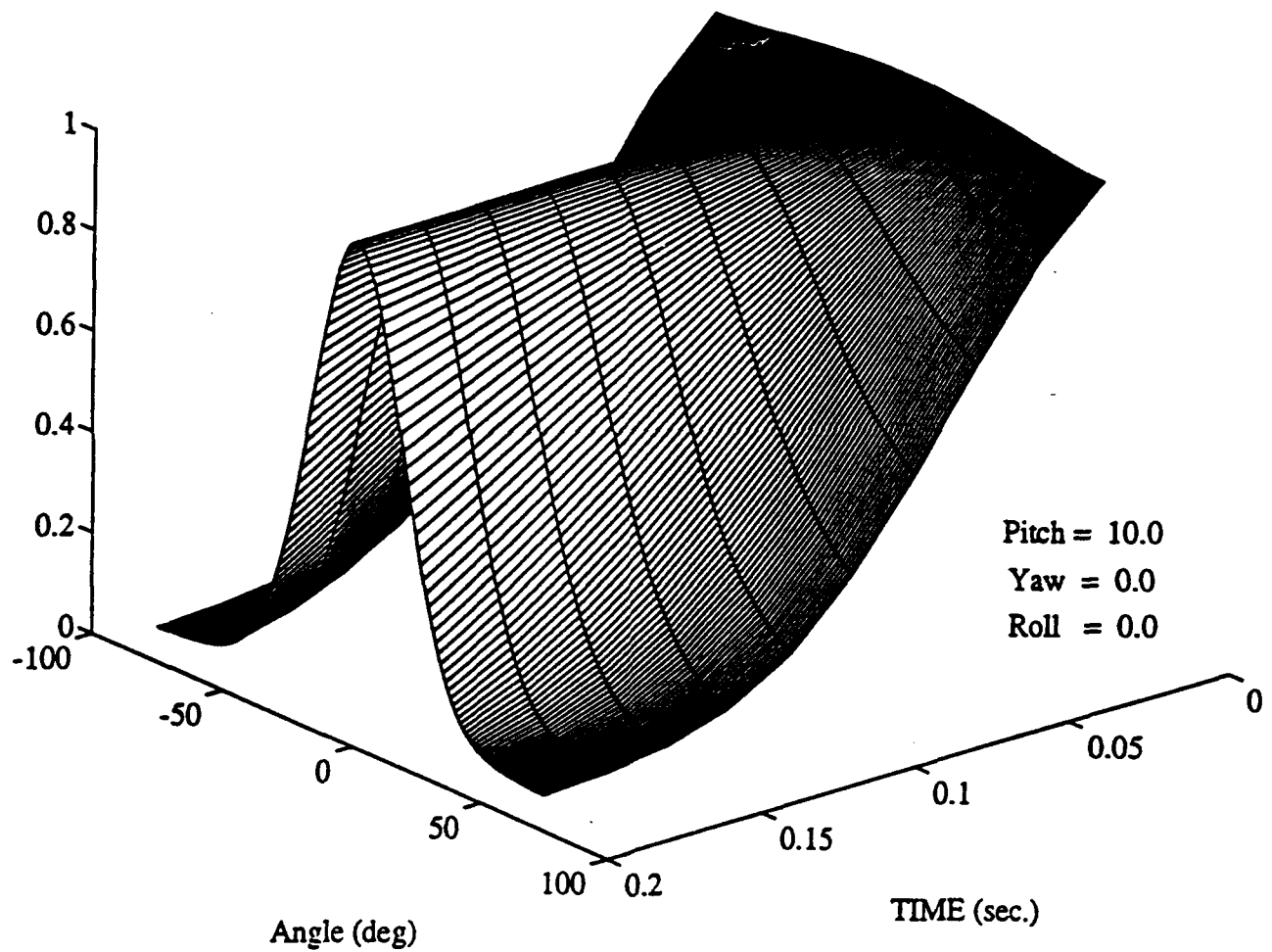


Figure 9 Vertical-motion-loss coefficient (VMC) for a pitch rate of 10 deg/s.

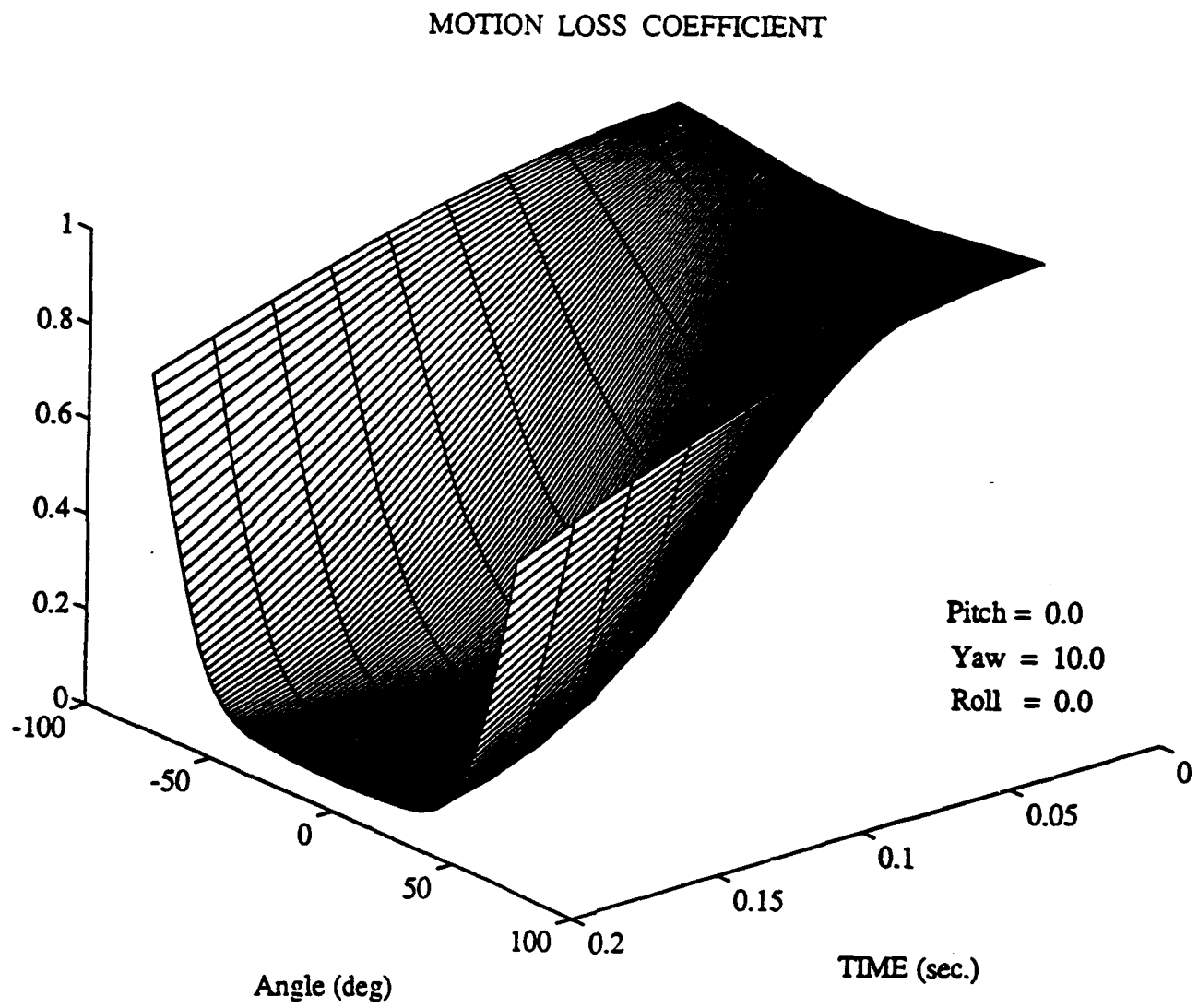


Figure 10 Vertical-motion-loss coefficient (VMLC) for a yaw rate of 10 deg/s.

MOTION LOSS COEFFICIENT

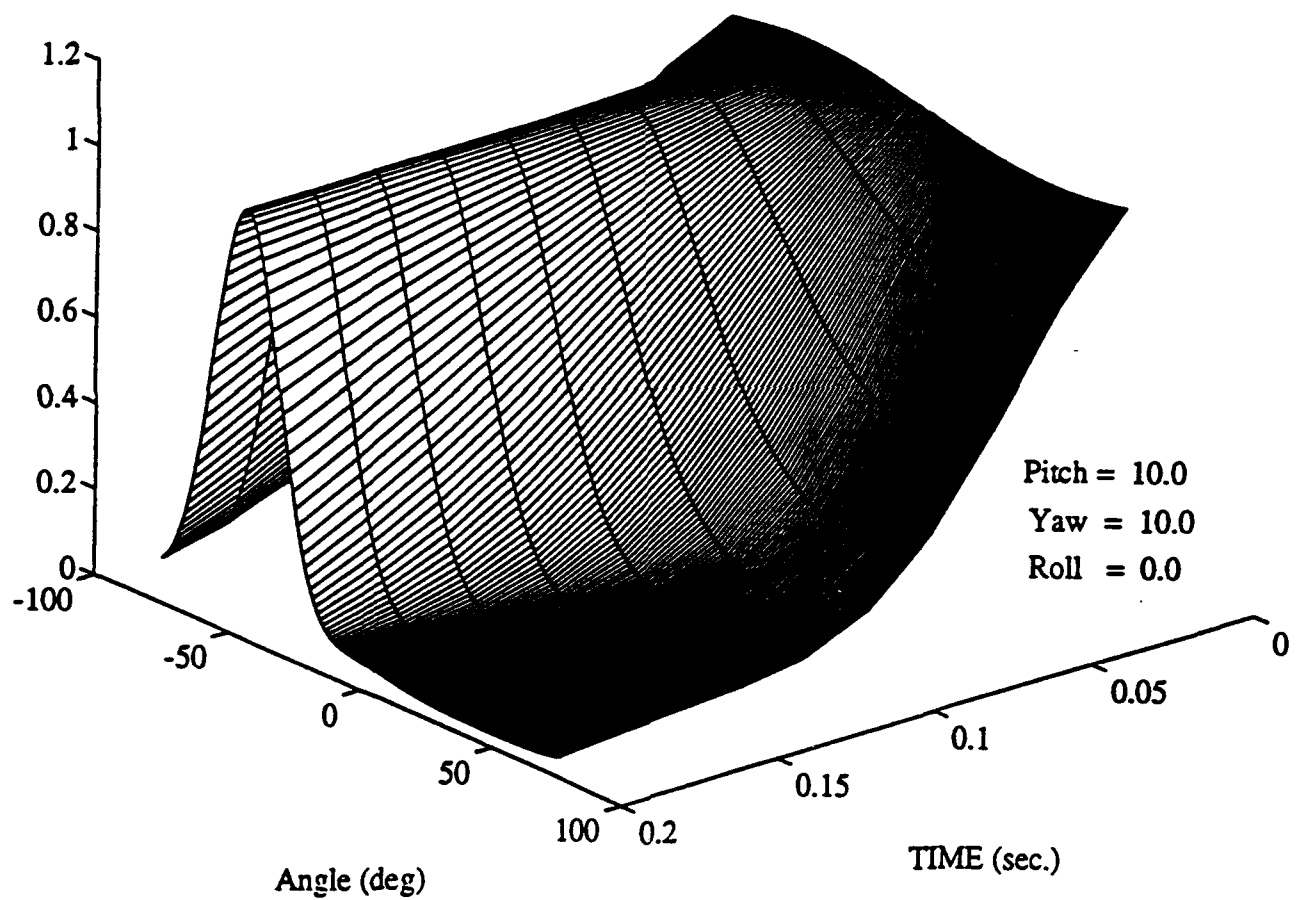


Figure 11 Vertical-motion-loss coefficient (VMLC) for a composite angular motion rates in pitch and yaw, each at 10 deg/s.

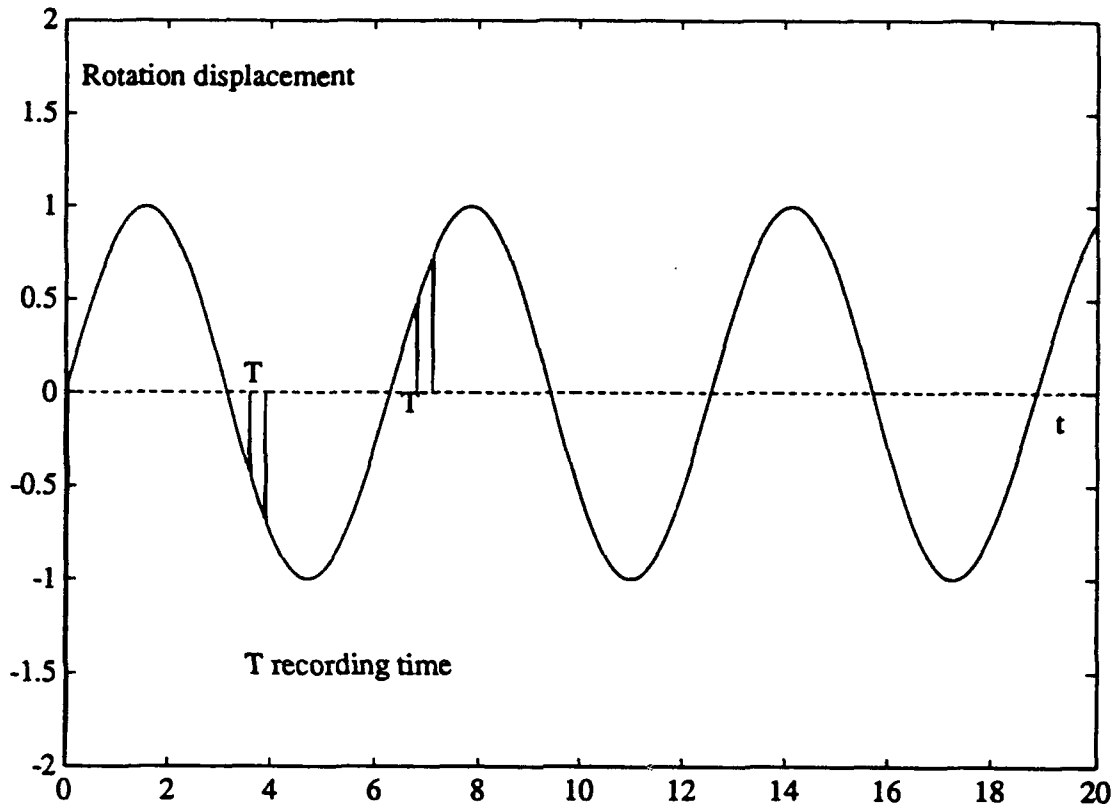


Figure 12 For a sample interval, T , angular motion is assumed constant.

slow change in platform motion, as shown in Fig. 12. If only angular measurements are available, instead of using angular rate measurements, we may use an approximate form for the angular rate,

$$W = \frac{\theta(k+1) - \theta(k)}{T} \quad (7)$$

where T is the elapsed time between the measurements of angular motion and k is the sample number.

3.3 Experimental Results

An experimental test was conducted during shallow-water work off the WHOI dock using a stepper motor mounted on the vehicle to rotate a forward-scan sonar (Fig. 2). Because of the narrow horizontal beamwidth of the forward-scan sonar, the test is equivalent to induced yaw motion of a sidescan (or forward-looking) sonar. The test was conducted in relatively calm water at a depth where surface-wave-induced motion was negligible. In this configuration the vehicle was static, and the stepping motor could be used to simulate induced yaw motions at a measurable and variable rate.

There are two program sequences that control the motor motion and the time between successive sonar pings. The first program commands the motor to remain at a fixed position while the sonar is pinging and collecting data; the second program allows the CPU to synchronize the pulse transmission with sonar scans so the receive beam is in constant motion during reception of a backscattered pulse.

The first data set corresponds to the sonar signal without motion loss; the second can be thought of as sonar data with a yaw-motion loss. We can then compute the SML by taking the ratio of these two data sets. By normalizing the backscattering cross section with respect to area (a range-dependent function of beam pattern and grazing angle), the continuous bottom return can be considered as resulting from a constant target strength over all ranges.

In our calculations, we simplify the problem by assuming that scattering is dominated by direct bottom and sea-surface backscatter, ignoring scattering contributions from other ray paths. For bottom backscattering, we use Lambert's law,

$$S_b = 10\log(\mu) + 20\log(\sin\theta) \quad (8)$$

where S_b is the bottom backscattering strength, μ is the bottom scattering constant, and θ is the grazing angle. For backscattering from the sea surface, we adopt Marsh's empirical model [3],

$$S_s = -36 + 40\log(\tan\theta) \quad (9)$$

where S_s stands for surface scattering. Figure 13 shows a typical BSM function with bottom and surface scattering. Since scattering from the surface (peak around vertical angle -50 deg) is much smaller than that from the bottom (peak around vertical angle 50 deg), we intentionally exaggerate the former by about 40 dB.

Figure 14 gives a comparison of the predicted SML with experiment results for a range of about 75 m (0.1 s on the time axis). Although the comparison is not exact, both data and the simulated SML show similar time dependence, which suggests that our motion-loss model is valid. The noisy SML is largely the result of restricting the scanning area to a small sector so that bottom inhomogeneities over larger areas would not detract from results.

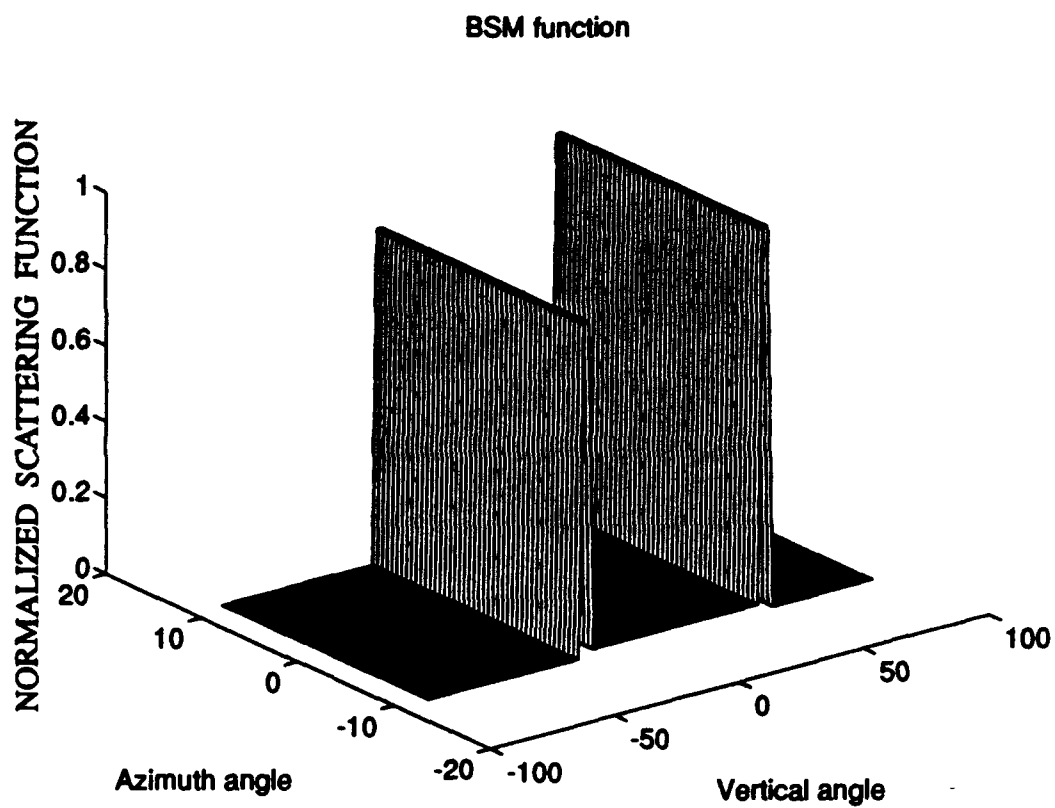


Figure 13 Typical backscattering-strength map (BSM) showing surface and bottom returns.

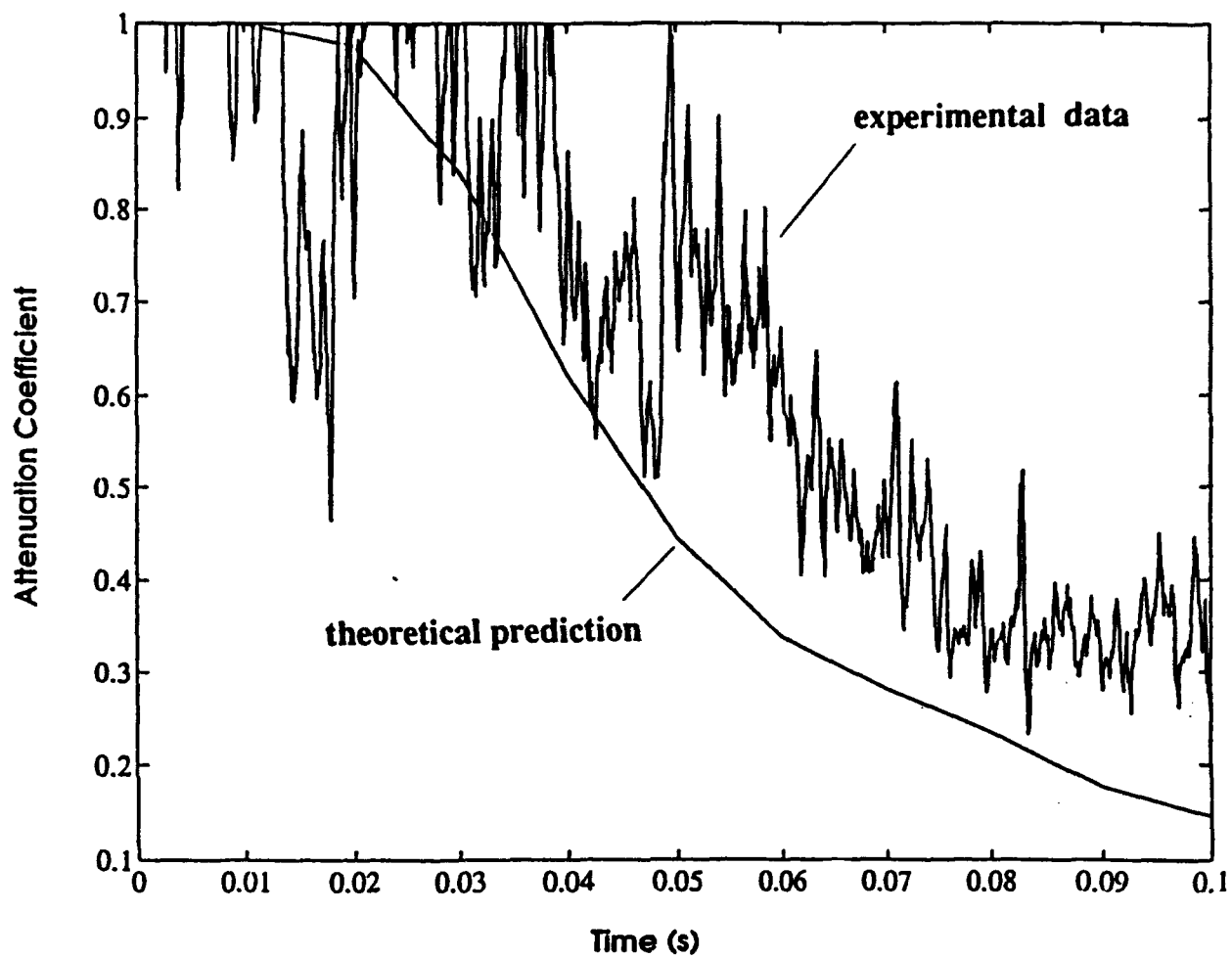


Figure 14 Comparison of predicted and experimental results for signal motion loss (SML) of a 300-kHz sonar using a backscattered bottom return.

4.0 REVERBERATION

4.1 Brief Description of the Acoustic-Reverberation Model

Difficult problems encountered in the study of sound propagation in a range-dependent shallow-water environment are mode coupling for low-frequency applications and waveguide multipath for high-frequency applications. So far, there is no exact solution even for an ideal wedge (homogeneous media with smoothed boundaries) with a penetrable bottom. Rough interfaces (sea surface and seabed) and inhomogeneities within both the water column and the sediment further complicate theoretical predictions. In addition, bubble scattering near the sea surface strongly depends on statistics of the rough interface and bubbles. The statistics are functions of time and such environmental factors as wind speed.

Thus, an acoustic reverberation model in a realistic shallow-water waveguide involves at least three separate issues: wave propagation in a penetrable waveguide, scattering from rough interfaces, and the volume scattering from bubbles and sediment inhomogeneities. Each of these is a difficult topic in underwater acoustics. A general acoustic-reverberation model should take into account not only the three separate aspects mentioned above but also the more complicated interactions among them.

It is impractical to obtain accurate predictions for such a problem, at least at the current stage. However, it is possible to use either a simplified model, an empirical model, or some combination of the two to approximately describe acoustic behaviors in a shallow-water environment. The model should encompass the essential physical processes and can be used to at least qualitatively address some of the basic acoustic issues.

It is not our intention to develop any "new" theoretical models but to adapt or modify some existing models to fit our purpose. The acoustic model used in this report incorporates the following assumptions:

- a) homogeneous water column;
- b) perfect reflection from sea surface (reflection coefficient is -1); and
- c) constant slope with small roughness compared to the footprint.

Other features of the current model include:

- a) accounts for multiple bounces (reflections), but only the first scattering either from the sea surface or from the ocean bottom;
- b) applies an empirical model to surface scattering;
- c) applies a composite-roughness model to bottom scattering, which includes empirical models for volume scattering and bottom attenuation; and
- d) assumes the separability between incident and scattering directions for scattering, i.e., $F_{scat}(k_i, k_r) = F_{bs}(k_i)F_{bs}(k_r)$, where F_{bs} is the backscattering function [8].

4.2 Theoretical Model

4.2.1 Propagation

Since the frequencies of interest in this study are relatively high (wavelength is much smaller than the scale of the shallow-water waveguide), a few eigenrays are adequate to describe the propagation of an acoustic wave. The geometry of our problem is depicted in Fig. 15a for bottom scattering and in Fig. 15b for surface scattering, where only four rays are shown for each case. Figure 16 illustrates the geometry of relevant parameters required by the model including propagation distance, outgoing and incoming angles, as well as incident and scattering angles. Variables in Fig. 16 are:

S_0	source location
R_0	receiver location
S_i	i^{th} order source images
R_i	i^{th} order receiver images
ψ	wedge angle
ϕ_{s0}	angular coordinate of source
ϕ_{r0}	angular coordinate of receiver
r_{s0}	radial coordinate of source ($OS_0 = OS_1 = OS_2$)
r_{r0}	radial coordinate of receiver ($OR_0 = OR_1$)
ϕ_s	angular coordinate of source image
ϕ_r	angular coordinate of receiver image
θ_r	reflection grazing angle
θ_1	incident grazing angle of bottom scattering
θ_2	scattering grazing angle of bottom scattering
h_s	z coordinate of source image (S_2A)
h_r	z coordinate of receiver image (R_1B)
γ_0	outgoing angle (transmit)
γ_1	incoming angle (receiving)
Δ	horizontal offset (AB)
l_x	horizontal distance between source image and the scattering point (AQ)
r_1	distance between the source image and the scattering point (total transmitting distance = QS_2)
r_2	distance between the receiver image and the scattering point (total receiving distance = QR_1)

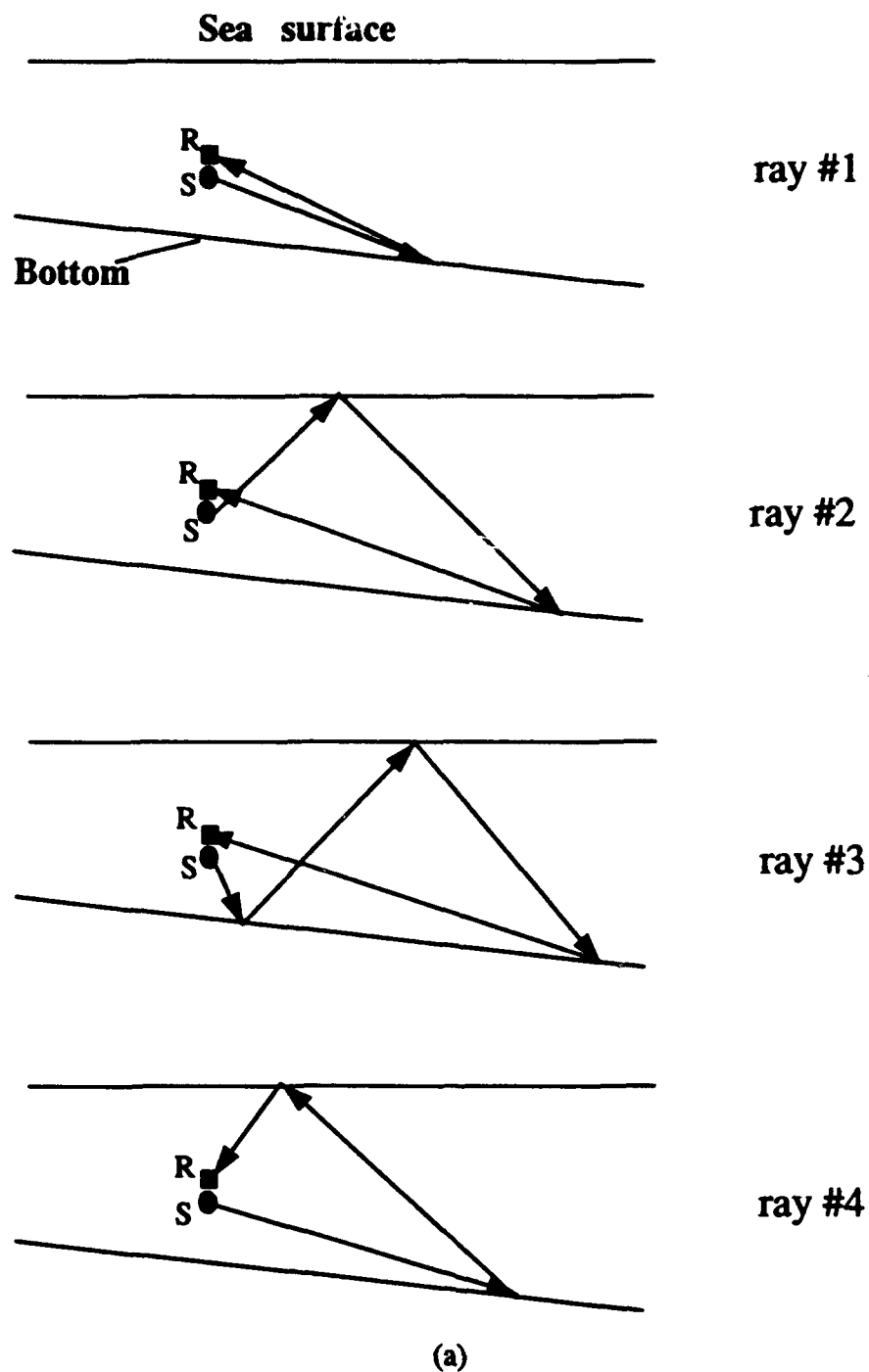


Figure 15 Geometry of bottom scattering ray paths in a shallow-water waveguide for down-slope propagation. For each case only four rays associated with first-order scattering are shown.

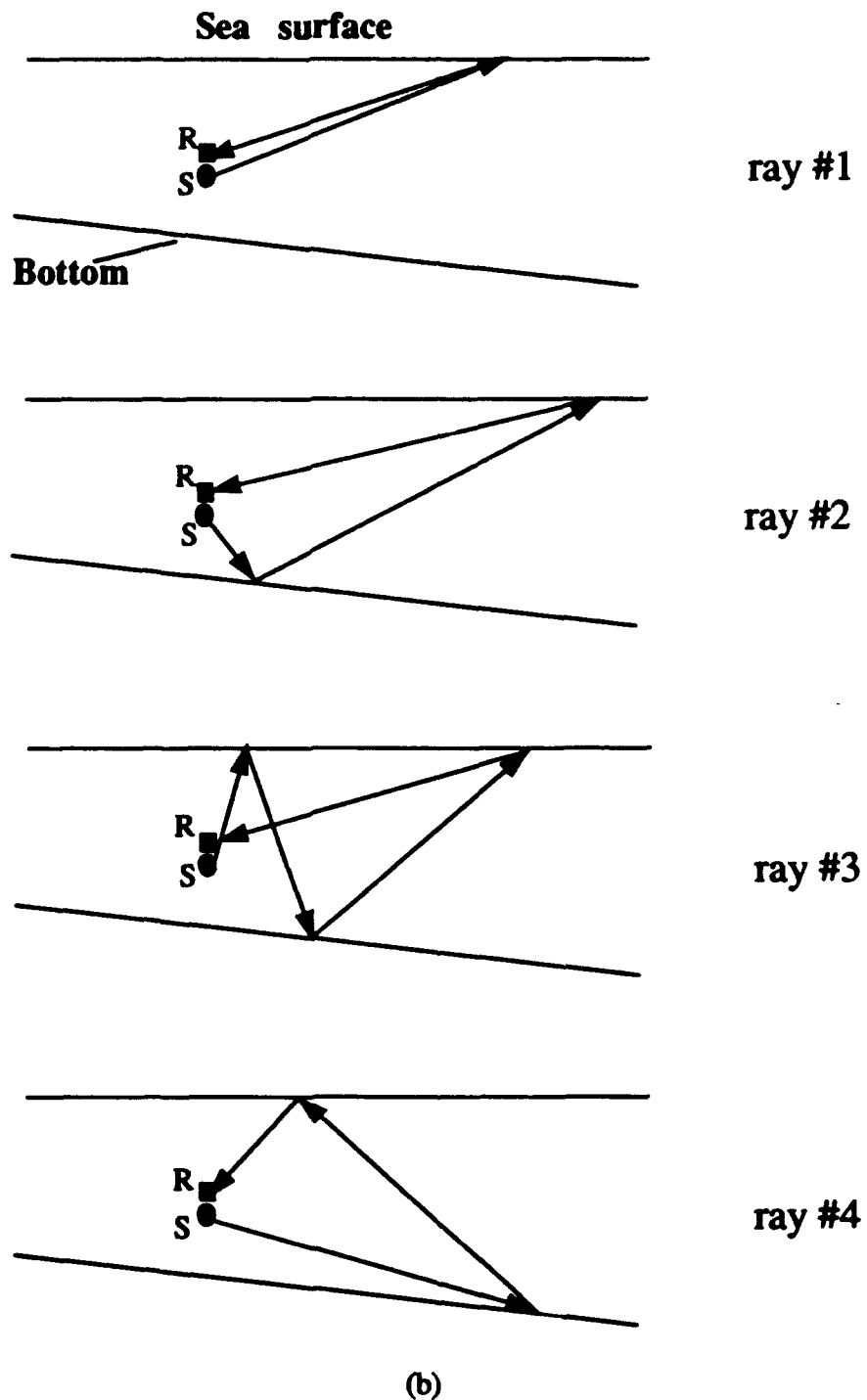


Figure 15 Geometry of surface scattering ray paths in a shallow-water waveguide for down-slope propagation. For each case only four rays associated with first-order scattering are shown.

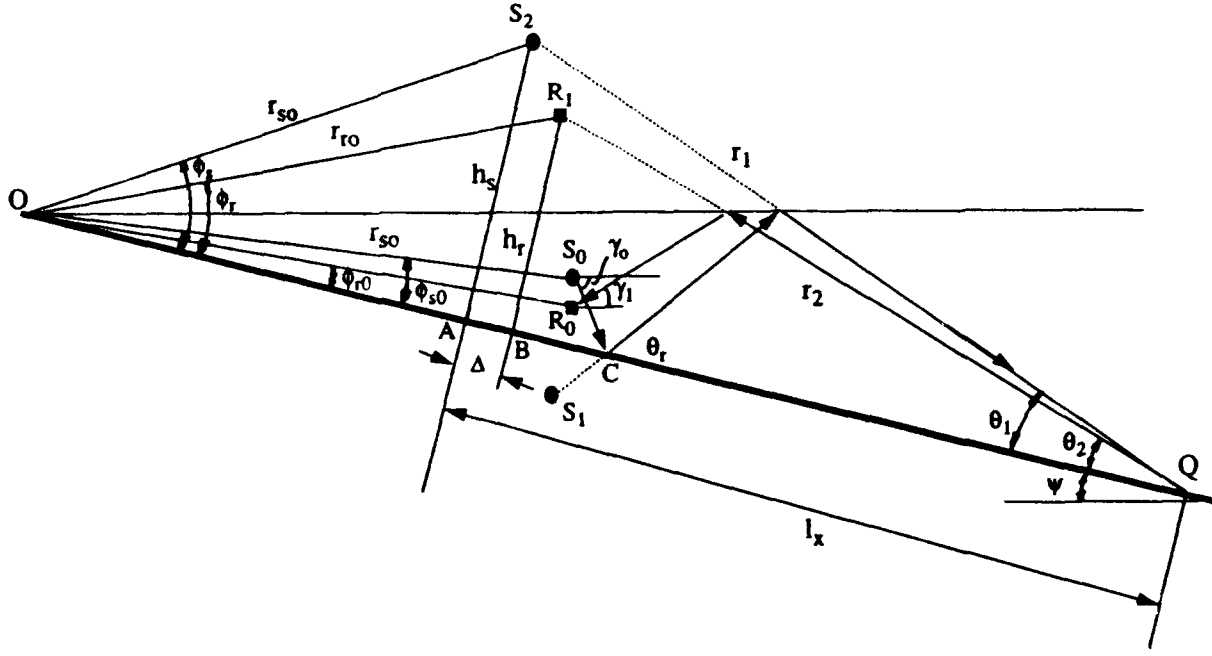


Figure 16 Geometry of a transmit ray showing relevant parameters.

Let $R = r_1 + r_2 = ct$, where c is sound speed and t is time, then

$$ct = \sqrt{h_s^2 + l_x^2} + \sqrt{h_r^2 + (l_x - \Delta)^2}, \quad (10)$$

where

$$\begin{aligned} h_s &= r_{s0} \sin \phi_s \\ h_r &= r_{r0} \sin \phi_r \\ \Delta &= r_{r0} \cos \phi_r - r_{s0} \cos \phi_s. \\ \phi_s &= 2\psi + \phi_{s0} \\ \phi_r &= 2\psi - \phi_{r0} \end{aligned} \quad (11)$$

Substituting variables from (11) into (10) and solving for l_x , we have

$$l_x = \frac{-B \pm \sqrt{B^2 - 4AC}}{2A}, \quad (12)$$

where

$$\begin{aligned}
 A &= 1 - \frac{\Delta^2}{R^2} \\
 B &= 2\Delta \left(\frac{M}{R} - 1 \right) \\
 C &= h_r^2 + \Delta^2 - M^2 \\
 M &= \frac{R^2 - h_s^2 + h_r^2 + \Delta^2}{2R}
 \end{aligned} \tag{13}$$

The plus and minus signs in (12) correspond to down-slope and up-slope propagation, respectively. We can now express other variables in terms of l_x as

$$\begin{aligned}
 r_1 &= \sqrt{h_s^2 + l_x^2} \\
 r_2 &= \sqrt{h_r^2 + (l_x - \Delta)^2}
 \end{aligned} \tag{14}$$

and

$$\begin{aligned}
 \theta_1 &= \text{atan} \left(\frac{h_s}{l_x} \right) \\
 \theta_2 &= \text{atan} \left(\frac{h_r}{l_x - \Delta} \right) \\
 \theta_r &= \theta_1 + 2\psi
 \end{aligned} \tag{15}$$

The ensonified area, ΔS , is

$$\Delta S = \phi_e r_1 \frac{c\tau}{\cos\theta_1} = \phi_e r_1 c\tau \frac{r_1}{l_x}, \tag{16}$$

where τ is the pulse length and Φ_e is the equivalent horizontal beamwidth. For a rectangular transducer, we use the relation given in [4],

$$10\log\phi_e = 10\log \frac{\lambda}{2\pi L} + 9.2, \tag{17}$$

where L is transducer length.

By combining the above results, the average reverberation intensity can be expressed in terms of the scattering coefficient, $F_{scat}(k_i, k_r)$, and the other geometric terms given by (14)-(17) as

$$I = \frac{F(\theta_1, \theta_2) e^{-\alpha(r_1 + r_2)}}{r_1^2 r_2^2} \Delta S R_b(\theta_r), \quad (18)$$

where θ_r is the reflection grazing angle, R_b is the reflection coefficient for a planar interface, and α is the attenuation constant. A more general expression including multiple bounces between the sea surface and the bottom can be obtained by replacing the reflection coefficient term in (18) appropriately.

The average reverberation intensity for surface scattering has the same form as (18). For convenience, in the surface-scattering configuration we use the sea surface as the horizontal axis. Minor modifications are needed to obtain the corresponding parameters in the new coordinate system.

4.2.2 Scattering

Because of inadequate studies in the area of bistatic scattering from a rough interface, a pseudobistatic approach [8] is used in our model. The scattering function, $F_{scat}(k_i, k_r)$, is assumed to have an approximate form,

$$F_{scat}(k_i, k_r) = F_{bs}(k_i) F_{bs}(k_r), \quad (19)$$

where F_{bs} is the backscattering function; k_i and k_r represent the incident and receiving directions, respectively. It is apparent that for backscattering (19) gives the correct answer. Although not accurate to describe bistatic scattering, it is satisfactory for our current study, as in most cases the eigenrays of direct bottom backscattering contribute most to the total scattering field.

For scattering from the sea surface, considering that transducers are mounted with a downward tilt in most cases, the beam pattern and inherent angular dependence of surface scattering make scattering from the sea surface insignificant when compared with the total scattered field, except at the instant when the transmitted signal just reaches the air-water interface, which results in a strong coherent-scattering component. Furthermore, the analytical expressions used to describe scattering from the sea surface are complicated because of the interactions between surface and volume scattering. Keeping these facts in mind, we use a simple empirical scattering model to approximate the scattering process by the sea surface. The model includes wind speed and bubble scattering effects. In our computer programs, there are options for several different empirical models [4].

For bottom scattering, we use the composite-roughness model to incorporate two-scale interface roughness, volume scattering of the sediment, and attenuation in the water and sediment. More detailed descriptions of this model can be found in [5], [6].

Figures 17 and 18 show the time series of reverberation level for up-slope and down-slope propagations with a source of unit intensity. In these figures the vertical transducer response is shown (i.e., for a normal sidescan-sonar geometry, the vehicle would be moving normal to the

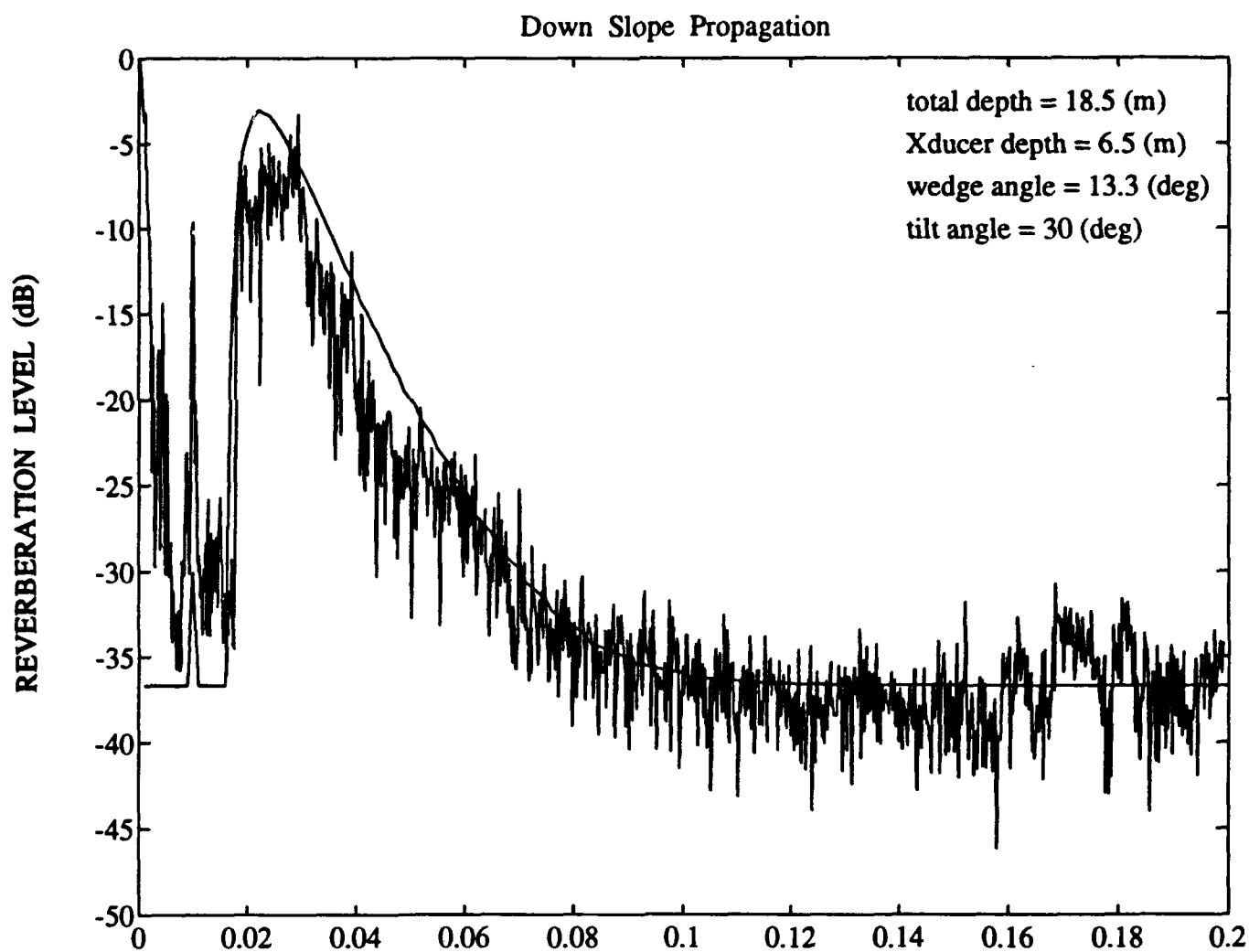


Figure 17 Time series of reverberation level (RL) for down-slope propagation in a shallow-water waveguide. The spiky curve is from experimental data; the smoothed curve is the theoretical prediction.

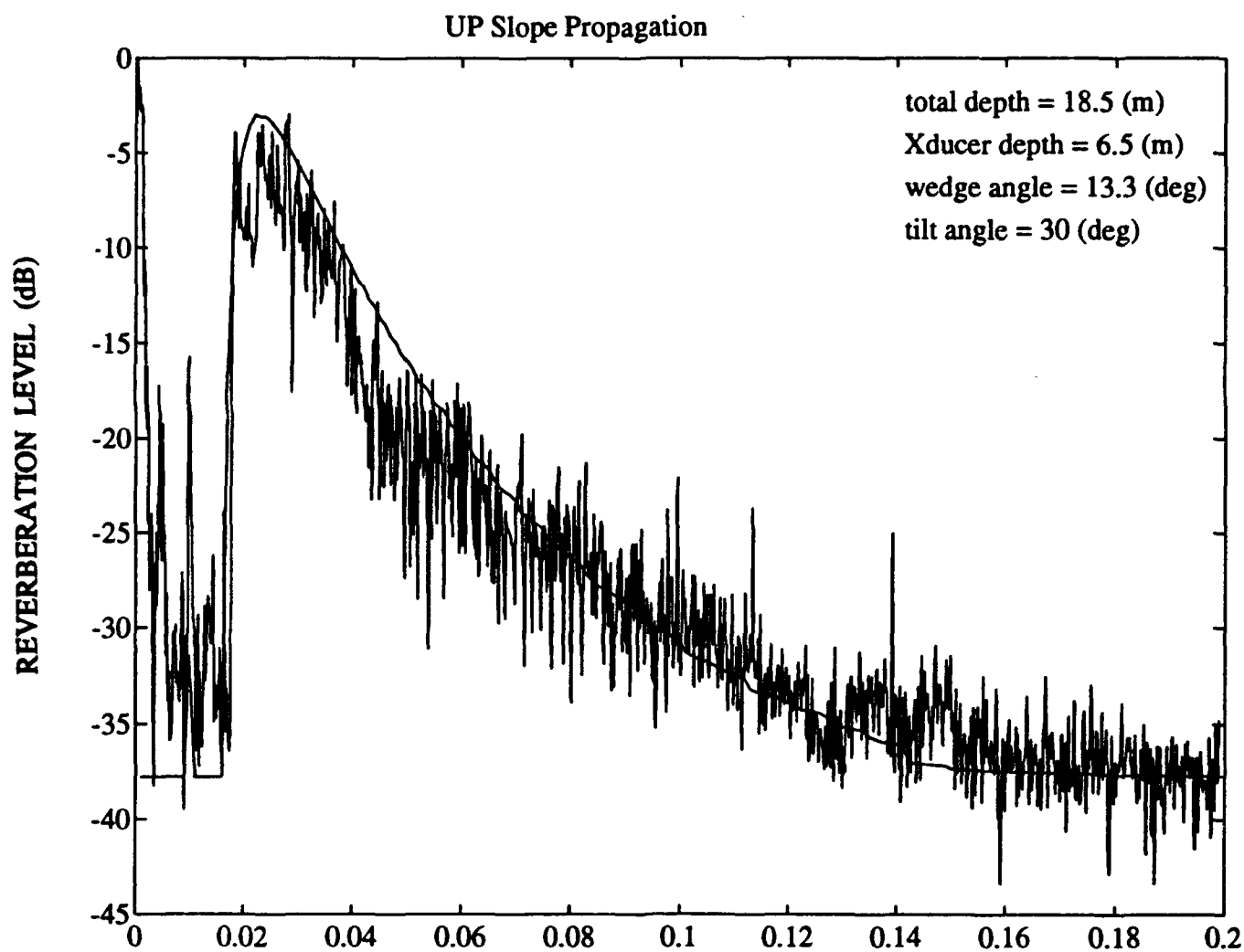


Figure 18 Time series of reverberation level (RL) for a up-slope propagation in a shallow-water waveguide. The spiky curve is from experimental data; the smoothed curve is the theoretical prediction.

page). The 0.2-s time series corresponds to a range of 150 m (300-m swath). Tilt angle denotes the transducer mounting angle from the horizontal plane (downward is positive). The spiky curves are experimental data collected off the WHOI dock; the smoothed curves are corresponding theoretical predictions.

Some parameters used in computations are indicated in the figures, while other parameters related to bottom and subbottom properties and required in the simulations are consistent with values given in [6]. Since the system was not fully calibrated, the absolute reverberation level was adjusted to obtain best fit. Although the absolute level is a free parameter in Figs. 17 and 18, the general trends of the reverberation curves agree with the experimental data reasonably well, which further confirms our acoustical model.

From Figs. 17 and 18 we can see that, as expected, the reverberation curve for up-slope propagation decreases more slowly than for down-slope propagation. With the same tilt angle for both up-slope and down-slope propagation, the angle between the incoming wave (resulting from direct bottom backscattering) and the beam axis is smaller for up-slope propagation than for down-slope propagation. A smaller angle results in less reduction in echo level due to the transducer beam pattern.

5.0 TARGET DETECTABILITY

In this section, we combine two models—motion loss and acoustic reverberation, both discussed separately in the previous sections—and investigate overall sonar performance in a shallow water environment. We calculate the effective vertical-beam-motion-loss coefficient (VMLC) defined in (6), then combine it with the 2-D vertical receiving beam pattern to form the effective vertical receiving beam pattern, which in turn is used by the reverberation-level (*RL*) algorithm.

We use an echo-reverberation ratio as a reference quantity to evaluate the sonar performance in terms of the detectable bottom swath width (DBSW). The echo-reverberation ratio represents the “signal” (backscattering cross section of target) to “noise” (spherical spreading, attenuation, and beam-pattern-compensated reverberation intensity) ratio, which is a measure of target detectability.

We use the DBSW as a composite measure of performance for the echo-mode detection of both midwater and bottom-proud targets. In this mode, a target is detectable if the echo-reverberation ratio exceeds a given detection threshold (DT). This measure does not address shadow-mode detection, where bottom reverberation levels must exceed surface reverberation plus ambient- and system-noise levels.

Although our model can be easily used to predict shadow-mode performance, our efforts in this report focus on echo-reverberation ratio for the purpose of demonstrating modeling capabilities. We also constrain our range of parameters and results to demonstrate modeling capabilities rather than to give an exhaustive analysis over all possible sonar systems and environmental conditions. Our aim has been to develop a tool for analysis that can be applied to other cases in support of a more focused proposal or design effort.

5.1 Echo-Reverberation Ratio

From the sonar equation, the echo-reverberation ratio can be expressed as the difference between echo level (*EL*) and reverberation level [4],

$$EL - RL = TS - (S_s + 10\log A), \quad (20)$$

where *TS* represents target strength, *S_s* denotes scattering strength, and *A* is the equivalent scattering area. Both terms on the right hand side include influences of vehicle motion as discussed in Section 3.0. Note that the second term on the right-hand side (in parenthesis) represents a pure scattering field.

Figure 19 illustrates such a pure scattering field for a particular case where a random noise background has been added. Since the noise is more or less stationary while the real backscattered signal from the surface or bottom is strongly range dependent, at larger ranges noise will dominate the total scattering field. Hence, the range and attenuation corrections in computing the scattering strength *S_s* in (20) result in an increased scattering field.

Although our program has the capability to model targets with different shapes and material properties at different orientations, for simplicity and consistency we use the same target throughout our analysis since the echo-reverberation ratio is a function of target strength for a given geometry. In the following examples we used a prolate spheroid of stainless steel with a

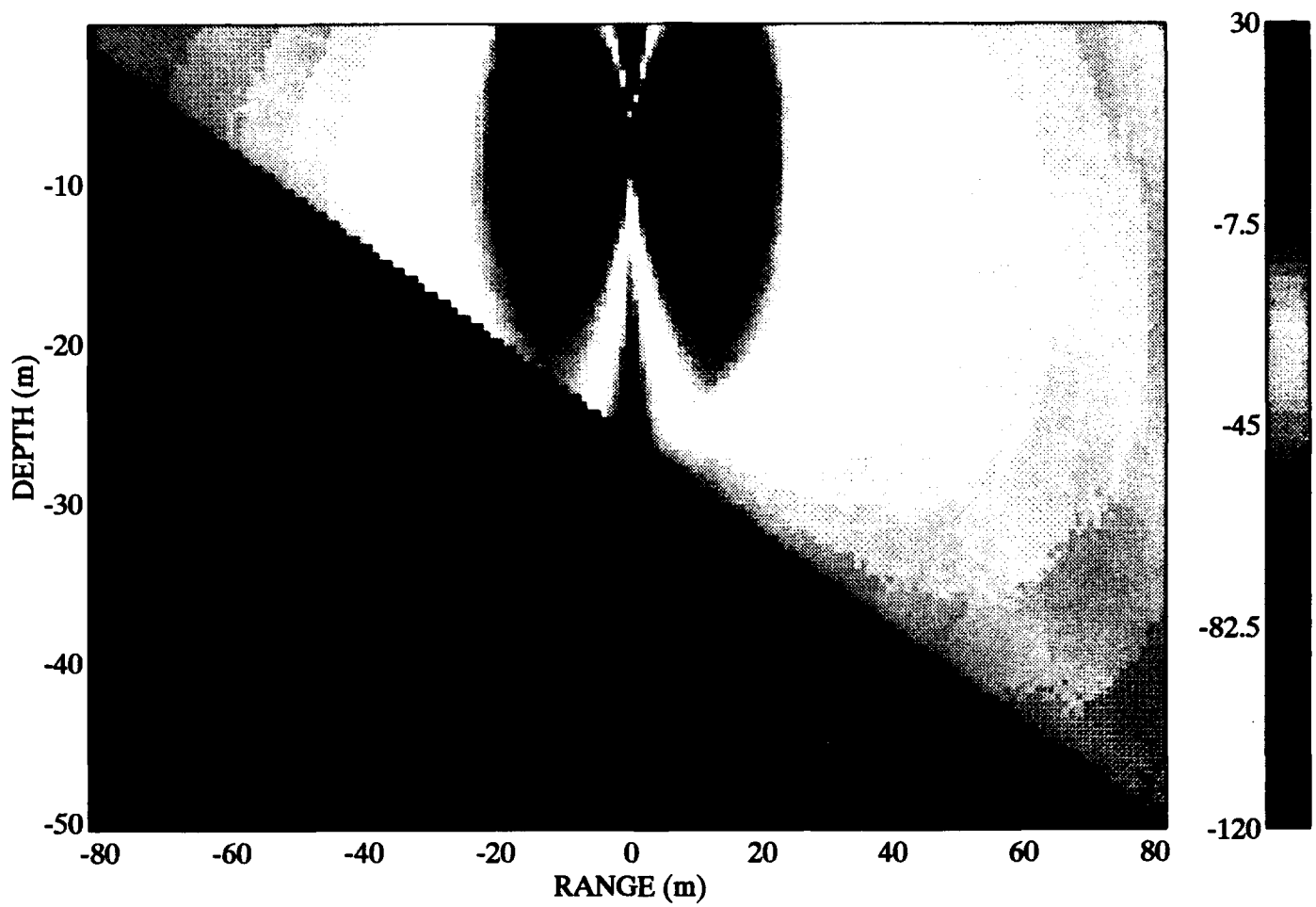


Figure 19 2-D image of echo level (EL) in a shallow-water waveguide. Slope is 0.3 (wedge angle 17.7 deg), tilt angle is 10 deg, 3-dB beamwidth is about 53 deg. Source and receiver are located at (0, -6.5).

broadside incidence. The target strength was calculated using a modified high-pass backscattering model [9]. Although the high-pass model smooths out all scattering structures, it can be considered a reasonable model as long as an averaging process is used [10]. More detailed studies of target scattering involving frequency and orientation dependencies can be found elsewhere [11]-[14].

Figure 20 shows the image plot of the echo-reverberation ratio, the contours of which are shown in Fig. 21. Figures 22-24 illustrate echo-reverberation-ratio contours for different cases; the open circle at zero range indicates source/receiver position (backscatter). Figure 22 shows that a narrower beamwidth gives a more directional detectable area (volume). When the transducer looks upward, more area (volume) in the upper water column is sensed (Fig. 23); looking downward, more area (volume) in the lower water column is sensed (Fig. 24).

To study the dependence of the target detectability more efficiently, we define DBSW as the swath width between the intersections of the ocean bottom with 6-dB echo-reverberation-ratio contour lines (horizontal distance between a and b in Fig. 24). We ignore the region near nadir, which results from a null of the transducer beam pattern. Although the DBSW is defined in terms of bottom coverage, this is only a convenient (and relevant) measure of performance. The trends identified in following results apply equally well to midwater targets.

5.2 Results and Discussions

All results shown in this subsection are only part of our sensitivity study but are representative in terms of DBSW. Initially there were 11 candidate variables considered important to our study: transducer depth; tilt angle (transducer mounting angle); transducer length and width, which control beam pattern; bottom slope; bottom depth; acoustic impedance contrast across the seafloor, which affects bottom scattering and reflection; wind speed, which affects surface scattering; and vehicle angular velocities (roll, pitch, and yaw).

Results for surface scattering are not shown since, according to early modeling, DBSW is almost unchanged with wind speed variation within a reasonable range, and DBSW plots are therefore featureless. Likewise, DBSW versus vehicle roll motion is not shown because, even though it affects the received echo level, it has little effect on DBSW. This is because both target strength and reverberation level are affected approximately proportionally due to the vehicle roll motion. Therefore, the following analysis focuses on the remaining nine candidate variables.

Figures 25-40 are representative results of our sensitivity study and show a family of three DBSW curves plotted against one of the nine candidate variables (variable 1). Each individual curve corresponds to a chosen value of one of the eight remaining candidate variables (variable 2). The other seven variables are held constant and set to reasonable default values listed in Table 1. In the following part we discuss the dependence of DBSW on all nine variables in more detail and explain the results in terms of the underlying physics.

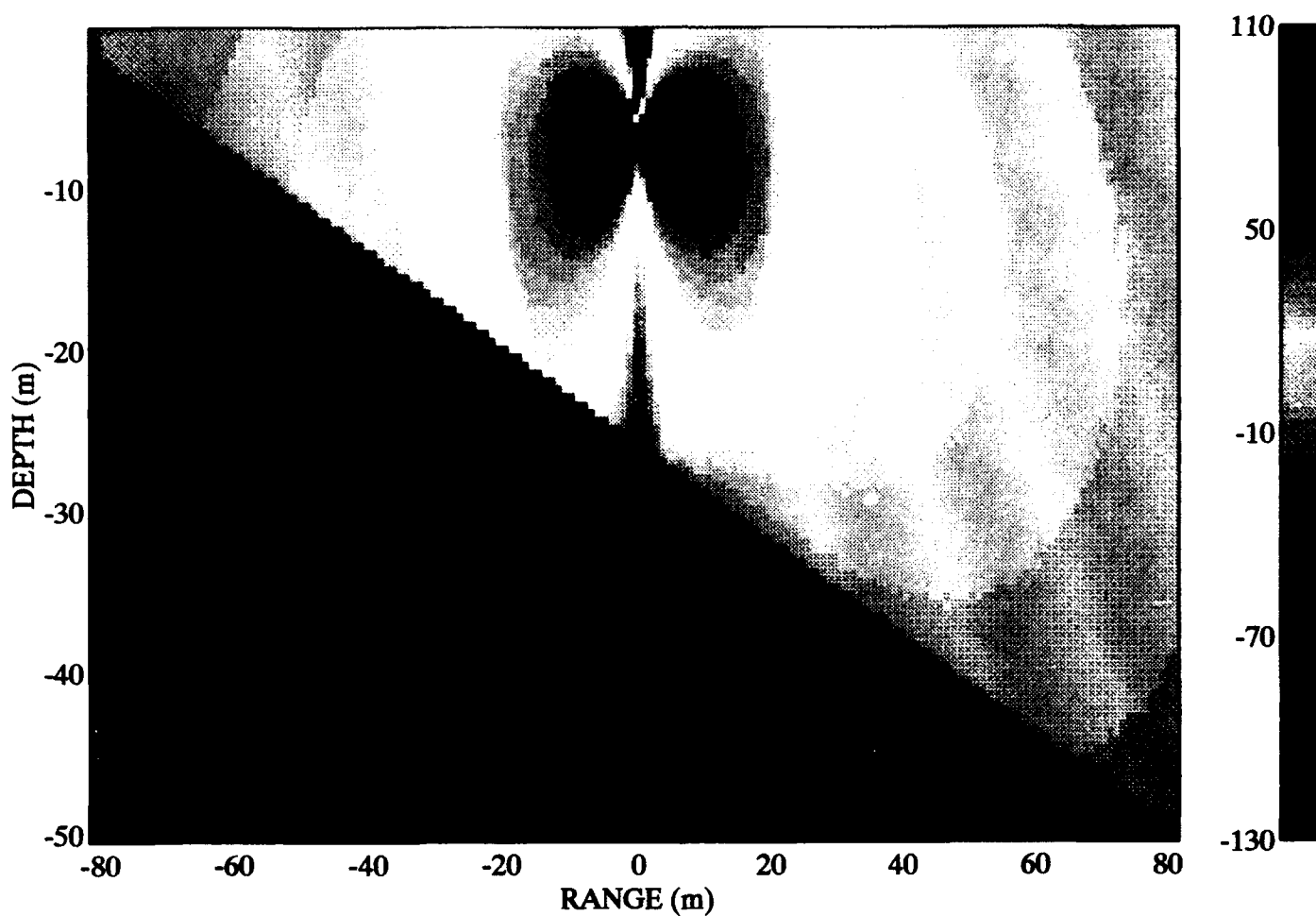


Figure 20 2-D image of echo-reverberation ratio in a shallow-water waveguide. All computational parameters are the same as in Fig. 19. The target is a stainless steel prolate spheroid of length 0.9 m with an aspect ratio 3:1. Target strength is computed on the assumption of broadside incidence.

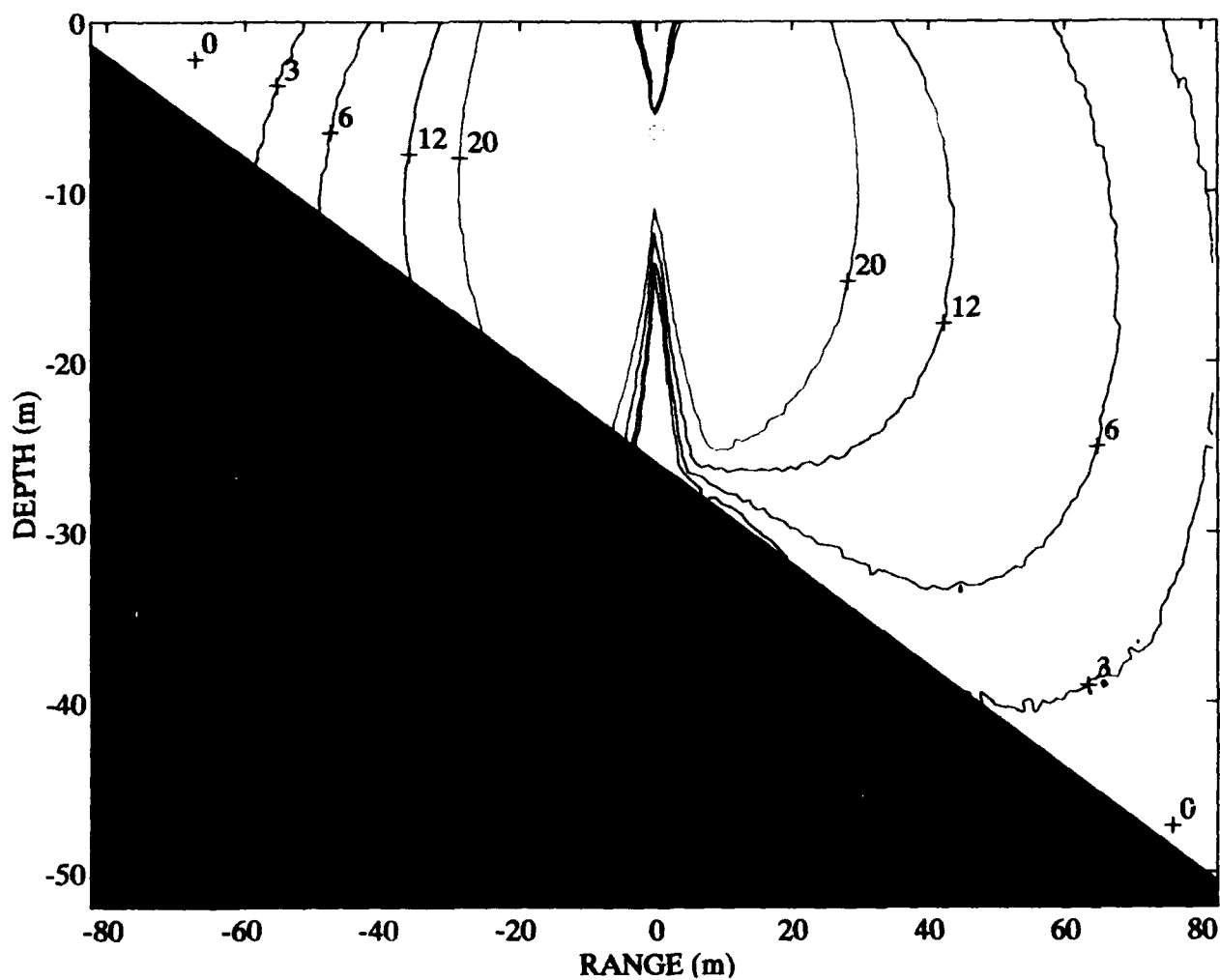


Figure 21 Echo-reverberation ratio contours using the same parameters as in Fig. 20. The open circle at zero range indicates the source/receiver location (backscatter).

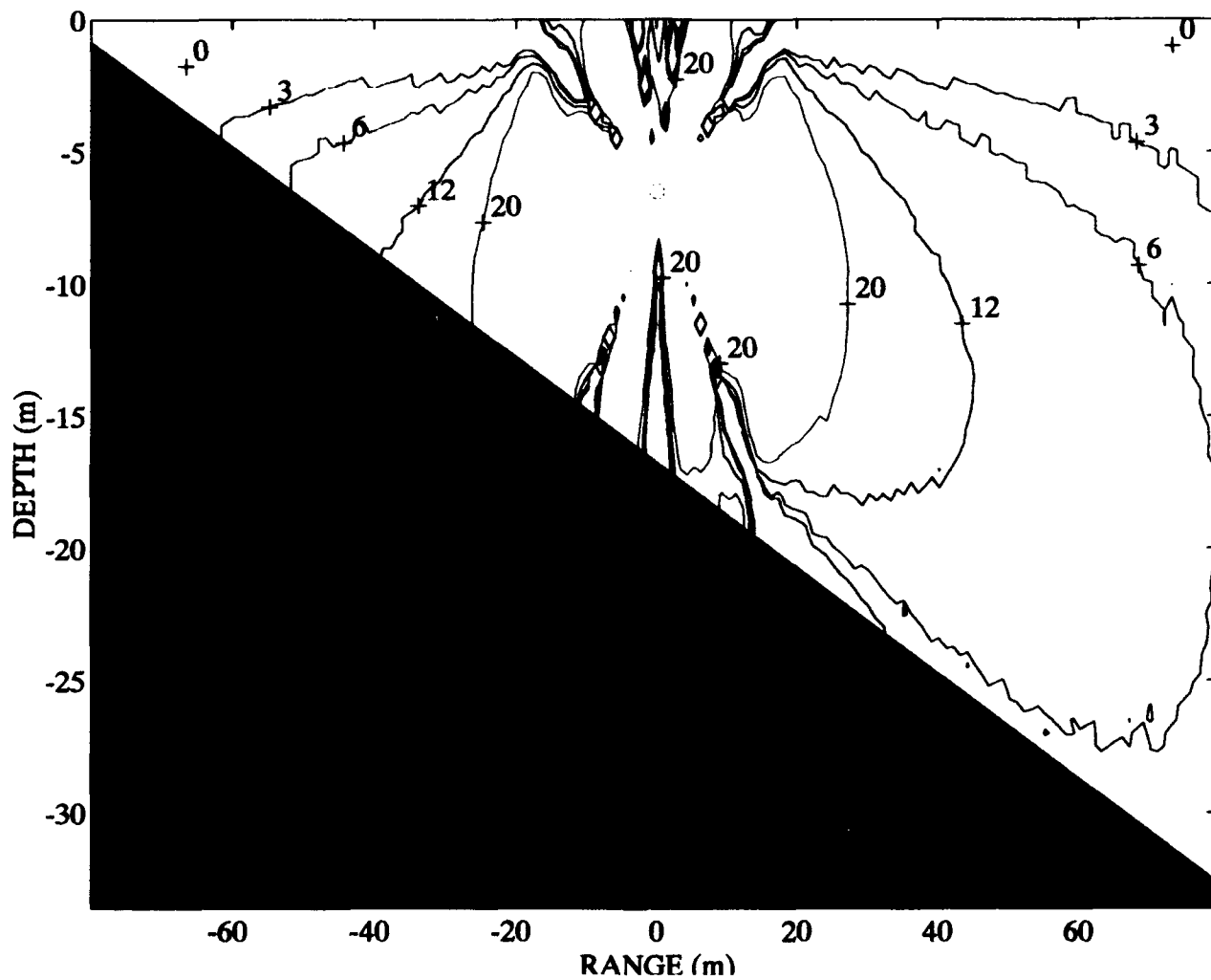


Figure 22 Echo-reverberation ratio contours for a slope of 0.3, tilt angle of 10 deg, and beamwidth of 27 deg. The open circle at zero range indicates the source/receiver location (backscatter).

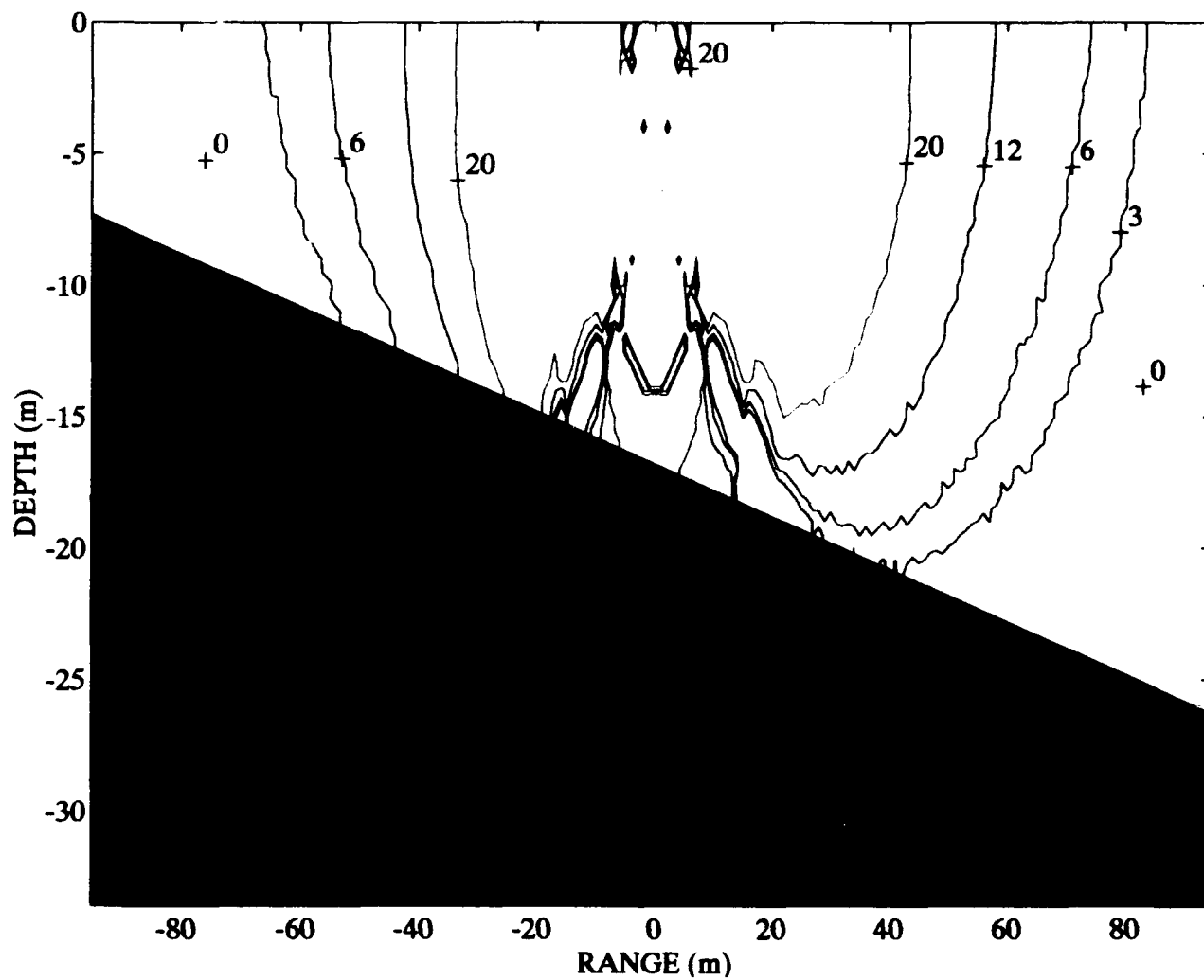


Figure 23 Echo-reverberation ratio contours for a slope of 0.1, tilt angle of -15 deg (looking up). The open circle at zero range indicates the source/receiver location (backscatter).

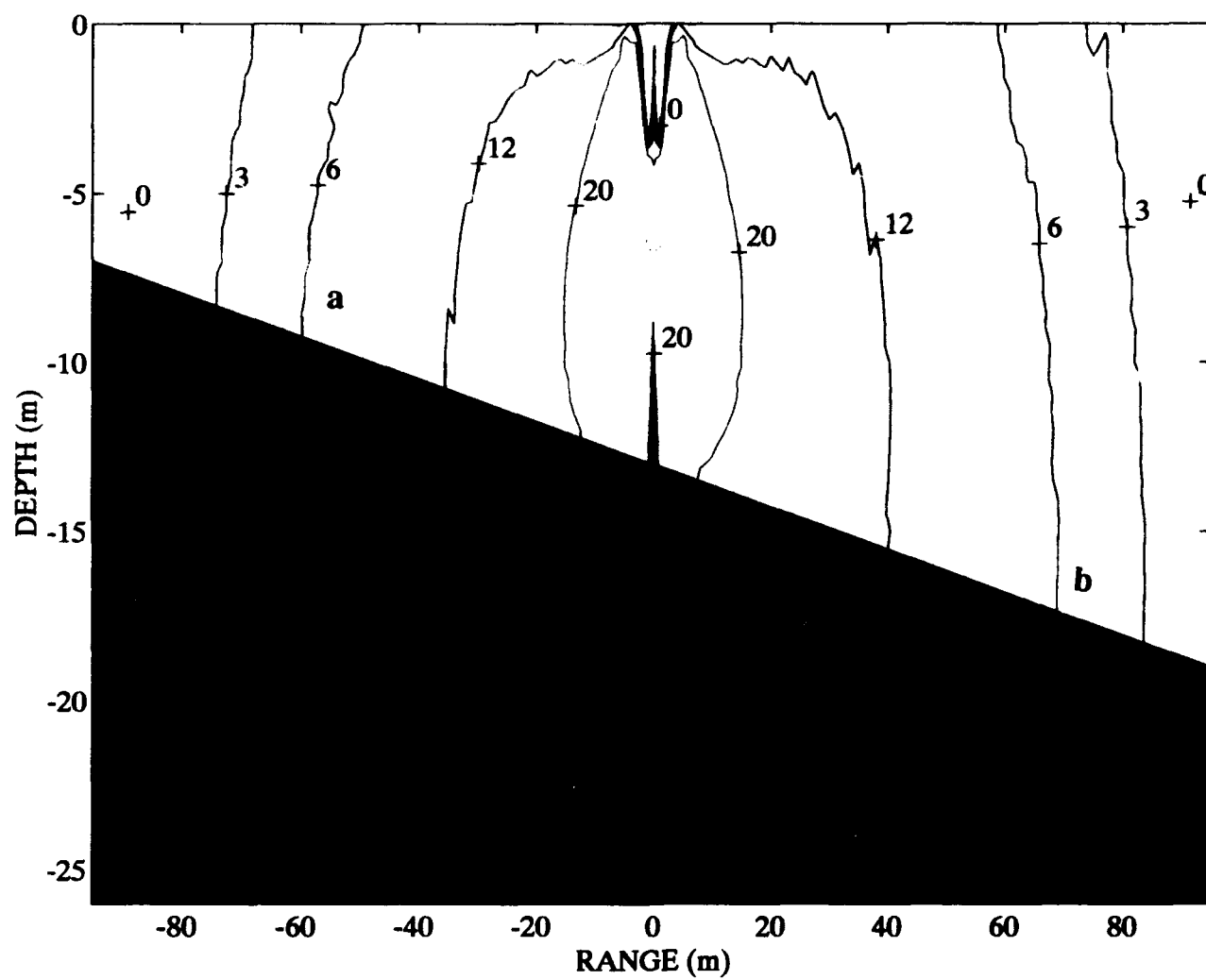


Figure 24 Echo-reverberation ratio contours for a slope of 0.063 (wedge angle 3.6 deg), tilt angle of 10 deg. The open circle at zero range indicates the source/receiver location (backscatter).

Table 1: Default Computation Parameters

Variable	Value
slope	0.1
total depth ¹	16.8 m
transducer depth	6.5 m
frequency	300.0 kHz
pulse length	200.0 μ s
transducer length	22.5 cm
transducer width	5.0 mm
tilt angle ²	10.0 deg
sound velocity (water)	1500.0 m/s
sound velocity (sediment)	1510.0 m/s
water density	1.0 g/cm ₃
sediment density	1.2 g/cm ³

1. depth at zero range ($x=0$)

2. transducer mount angle; downward is positive

5.2.1 Transducer Depth (Figs. 25 and 36):

In general, DBSW increases as the transducer position moves closer to the bottom. This feature can be understood easily by realizing that as the transducer approaches the bottom, for a constant range corresponding to a particular time, the backscattering grazing angle decreases, which produces a weaker scattering background. Thus, the signal-to-noise ratio increases and results in a larger DBSW.

It is interesting that there are discontinuities observed in Fig. 36 (solid line). Such a discontinuity is caused by the sudden separation and touching between the 6-dB contour lines and the sea bottom. This phenomenon can be seen clearly in Figs. 21-23, where the 6-dB contours are just above the ocean bottom on the down-slope side. There are many places where such discontinuities occur in other figures.

5.2.2 Tilt Angle (Figs. 26, 27, and 40):

DBSW increases as the tilt angle increases. It is obvious that more "volume" near the bottom can be ensonified or sensed with the transducer tilted downwards.

5.2.3 Transducer Width—Vertical Beam Pattern (Figs. 25, 26, and 28-30):

DBSW increases as the transducer width increases (vertical beamwidth decreases). Narrower vertical beamwidth results in less scattering from the ray paths going out/coming in along the directions away from the beam-axis. Thus, the total scattered field decreases and for transducers tilted facing down (positive tilt angle) DBSW increases.

5.2.4 Transducer Length—Horizontal Beam Pattern (Figs. 28, 31, and 37):

Increase in transducer length is equivalent to a narrower horizontal beamwidth and a smaller ensonified area. This eventually manifests itself as less scattering from both the bottom and the sea surface, resulting in a larger DBSW.

5.2.5 Vehicle Motion:

There are three different results with respect to different vehicle motions:

- (a) DBSW decreases as yaw speed increases (Figs. 29, 34, and 35);
- (b) DBSW increases as pitch speed increases (Figs. 31, 32, and 38); and
- (c) DBSW is insensitive to roll speed (not shown).

For case (a), with the given transducer beam patterns, the larger the speed of motion the smaller the overlapped volume between transmitting and receiving beam patterns. Since at any particular time the motion loss is maximum in the direction of the beam axis (Fig. 10), the reduction in scattered field comes mainly from the direct bottom backscattering, whose path is around the beam axis. At the same time, since we detect swath width at the bottom, the signal scattered from the target (assumed to be located at the bottom) decreases at the same rate as that from the direct bottom backscattering, while scattering along other ray paths decreases less than that from the ray path along the beam axis (i.e., due to vehicle motion the percentage reduction of the total

scattered field without the scatterer is less than the percentage reduction in the target strength). This unbalanced reduction causes a lower signal-to-noise ratio and results in a smaller DBSW.

Another interesting phenomenon is that a larger target gives a stronger dependence of DBSW on yaw speed. This can be seen by comparing Fig. 34 with Fig. 35, where the volume of the target used in Fig. 35 is about 16 times as large as that used in Fig. 17. When a larger target is used, the DBSW becomes larger and its detectable boundary corresponds to a later time and a lower reverberation level. Hence, the noise contribution to the total scattered field becomes more important. Because the noise field is independent of motion, the reverberation (noise) background remains unchanged or is slightly reduced. On the other hand, the backscattered signal from the target is also reduced due to the vehicle motion, but as a percentage it is more than that for the reverberation background. Hence, the signal-to-noise ratio decreases faster than in the smaller target case.

For case (b) (pitch), the motion loss is minimum along beam axis (Fig. 9). Following the discussions for case (a), we can conclude that the percentage reduction of total scattered field in the waveguide without the scatterer is larger than that from a single target. Thus, a larger DBSW is expected.

For case (c), although roll changes the received signal level, it also simultaneously changes the received signal from the target. In addition, since the vertical beamwidth is much larger than the horizontal, in contrast with case (4), the equivalent beam pattern due to roll doesn't change very much unless the speed of motion is very large. Therefore DBSW remains virtually unchanged.

5.2.6 Bottom Scattering (Figs. 33 and 39):

DBSW in general decreases as acoustic-impedance contrast increases, but the dependency is weak as the bottom scattering is relatively insensitive to the impedance contrast at the seafloor interface for small grazing angles.

5.2.7 Bottom Slope (Figs. 27, 30, 32, and 34-39):

DBSW decreases as slope increases (Note that the actual slope is negative. For simplicity, we use absolute value of slope throughout this report). As the slope increases, backscattering grazing angle increases for up-slope propagation and decreases for down-slope propagation. An increase or a decrease in grazing angle causes a decrease or an increase, respectively, in the backscattering field. As discussed in Section 4.2.2, reverberation for up-slope propagation decreases more slowly than for down-slope propagation; hence, the change in scattering field due to slope on the up-slope propagation side appears to be more important than that on the down-slope propagation side. Thus, it is expected that the amount of decreased DBSW on the up-slope propagation side is larger than the amount of increased DBSW on the down-slope propagation side.

5.2.8 Bottom Depth (Figs. 33 and 40):

It is observed that DBSW decreases as bottom becomes deeper. As bottom depth increases, for a fixed range, the backscattering grazing angle at the bottom is larger than that with a shallower bottom. The increased backscattering field due to a larger grazing angle results in a smaller DBSW.

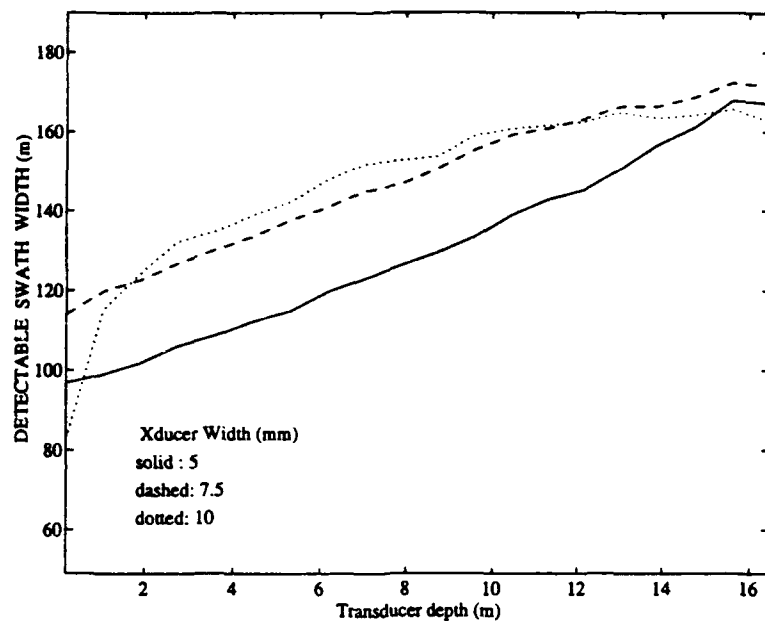


Figure 25 Detectable bottom swath width (DBSW) as a function of transducer depth and transducer width.

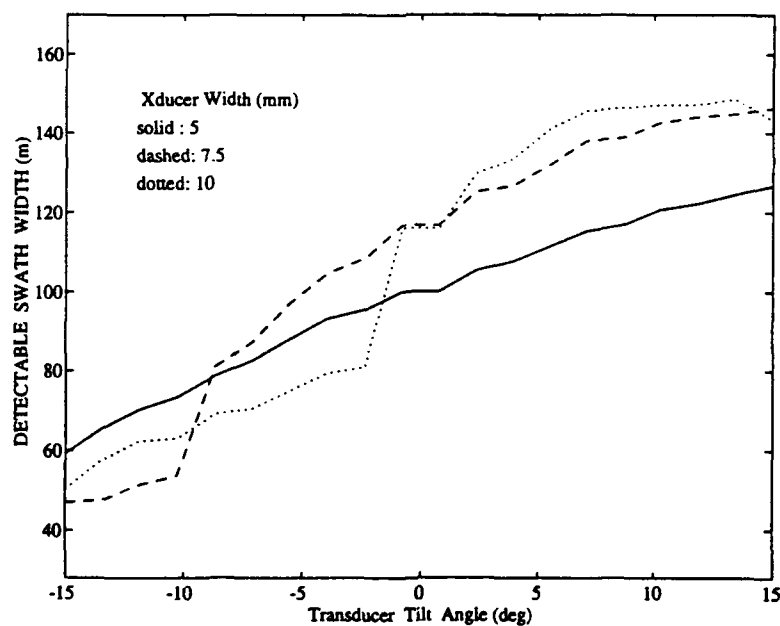


Figure 26 Detectable bottom swath width (DBSW) as a function of transducer tilt angle and transducer width.

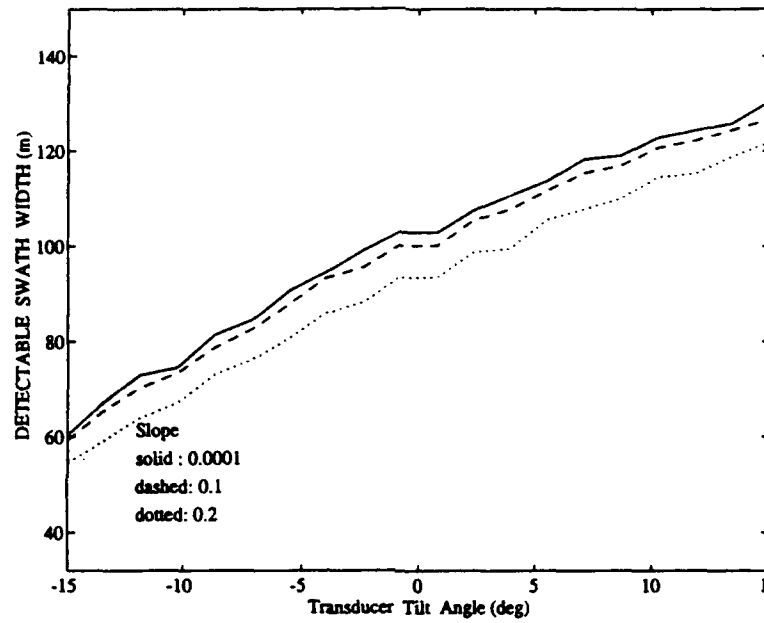


Figure 27 Detectable bottom swath width (DBSW) as a function of transducer tilt angle and bottom slope.

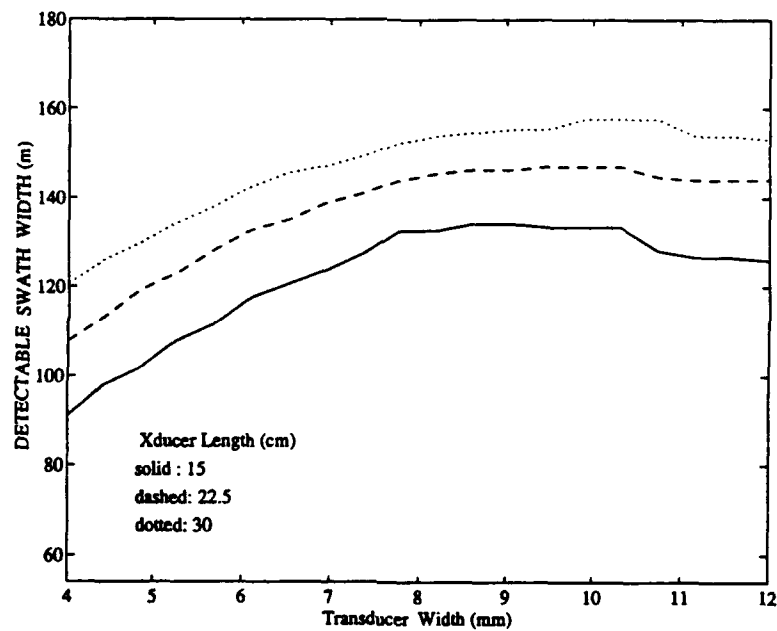


Figure 28 Detectable bottom swath width (DBSW) as a function of transducer width and transducer length.

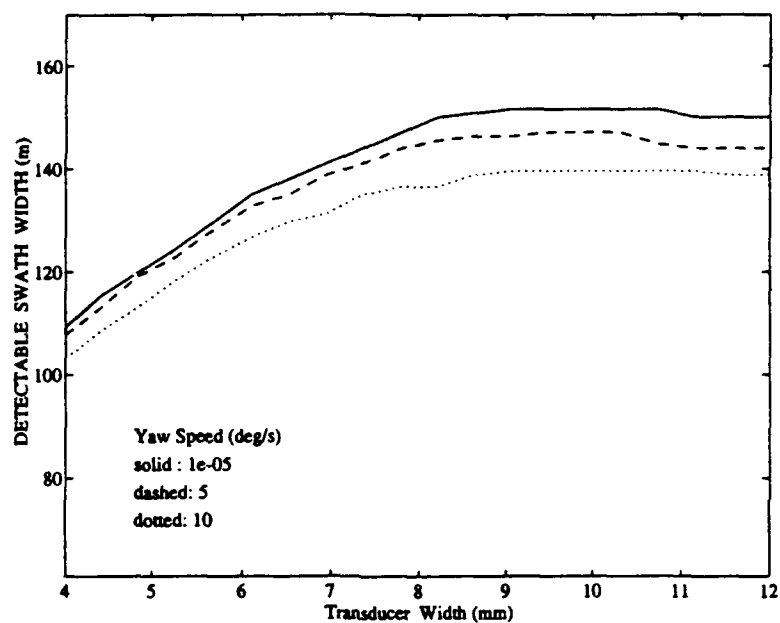


Figure 29 Detectable bottom swath width (DBSW) as a function of transducer width and yaw rate.

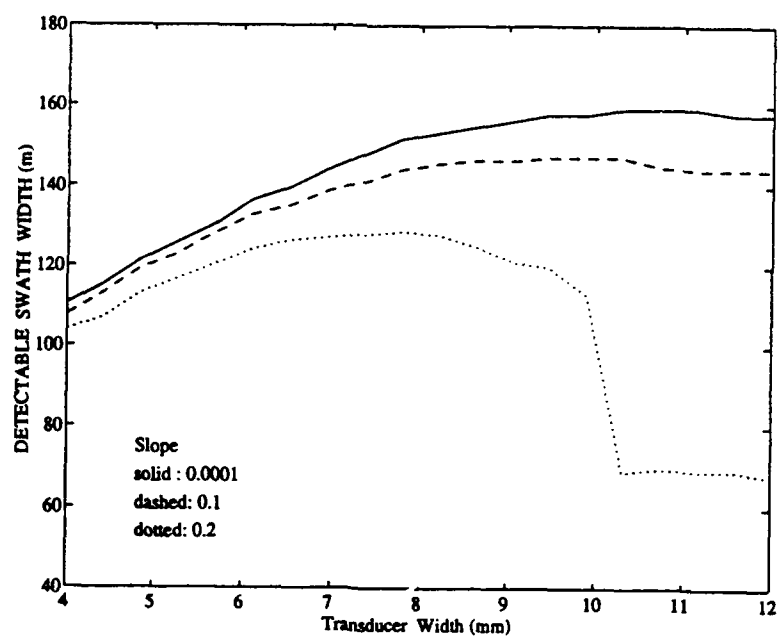


Figure 30 Detectable bottom swath width (DBSW) as a function of transducer width and bottom slope.

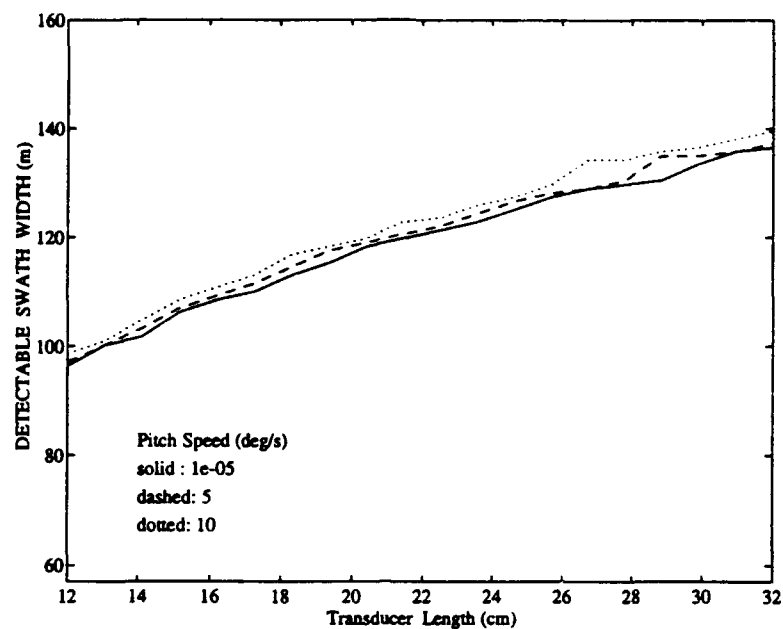


Figure 31 Detectable bottom swath width (DBSW) as a function of transducer length and pitch rate.

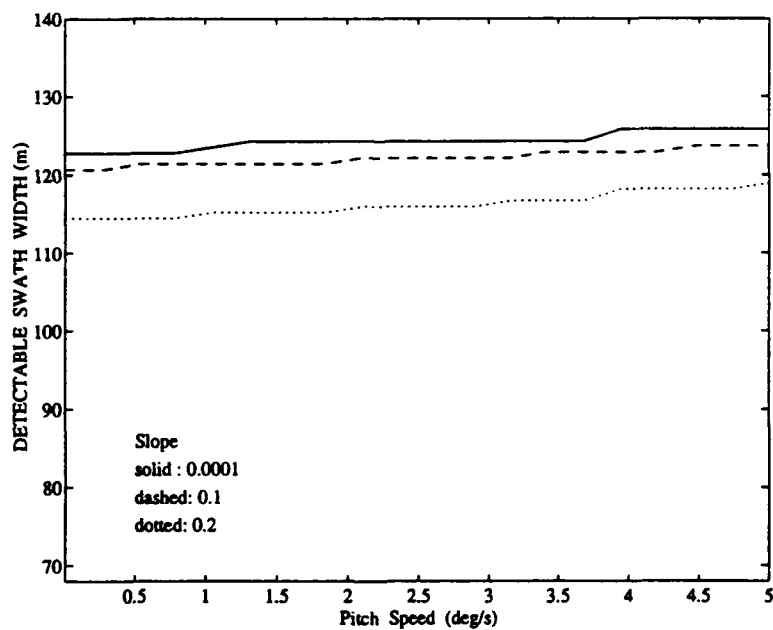


Figure 32 Detectable bottom swath width (DBSW) as a function of pitch rate and bottom slope.

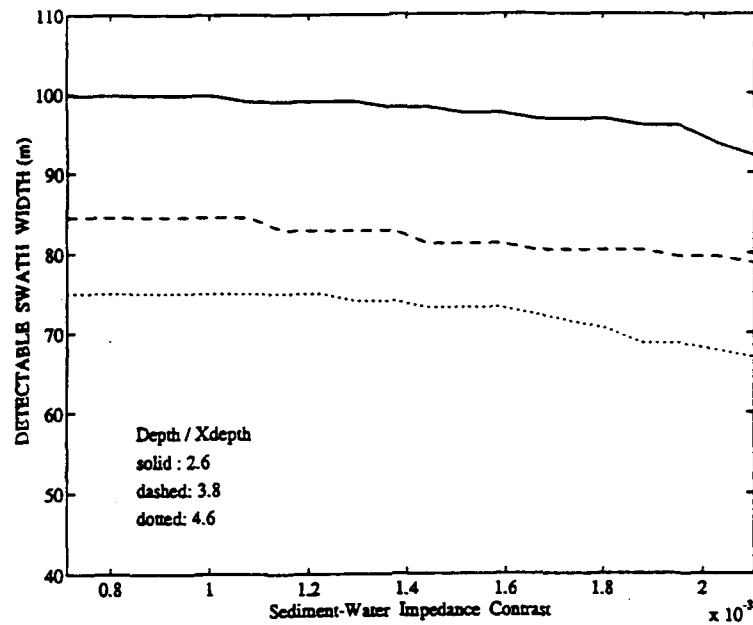


Figure 33 Detectable bottom swath width (DBSW) as a function of sediment-water impedance contrast and normalized depth (depth/Xdepth).

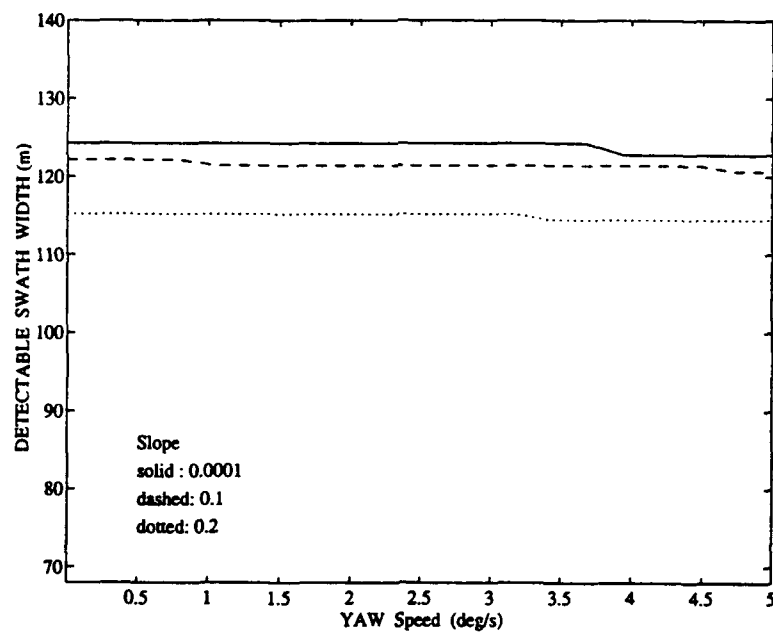


Figure 34 Detectable bottom swath width (DBSW) as a function of yaw rate and bottom slope.

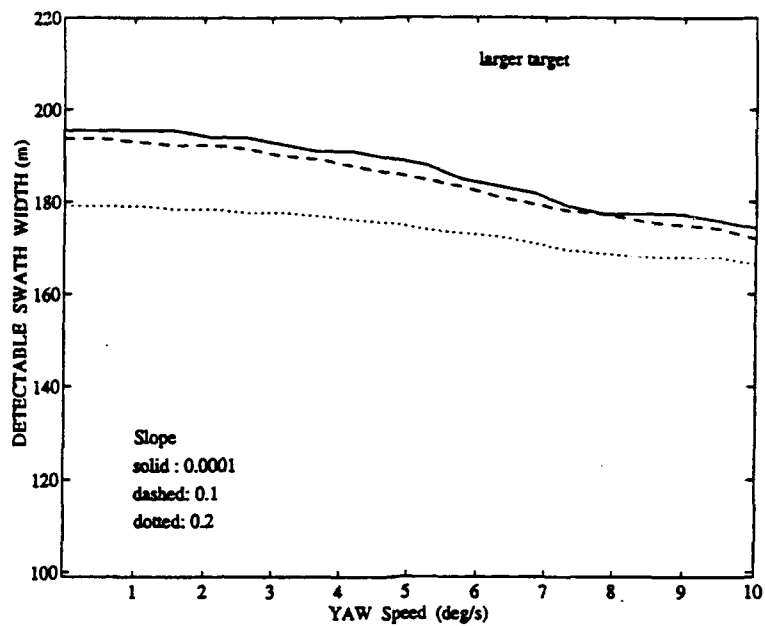


Figure 35 Detectable bottom swath width (DBSW) as a function of yaw rate and bottom slope (laser target).

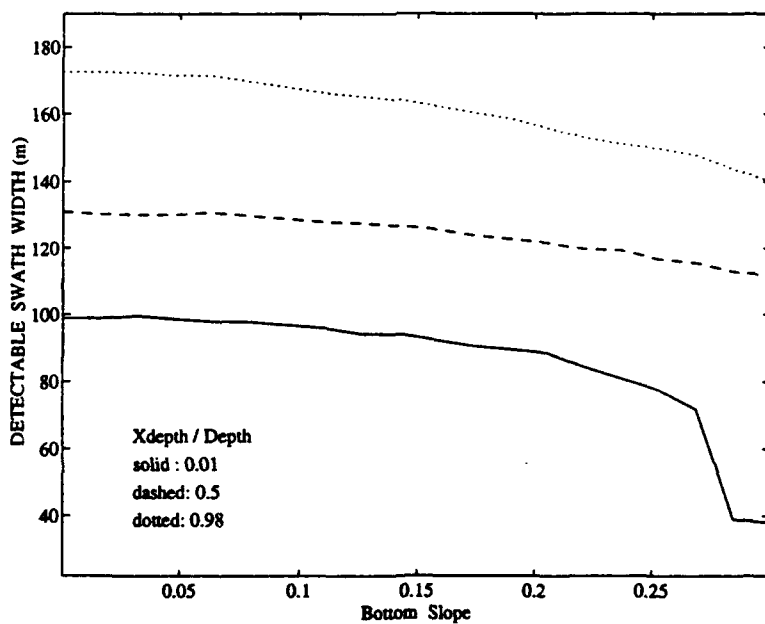


Figure 36 Detectable bottom swath width (DBSW) as a function of bottom slope and normalized transducer depth (Xdepth/depth).

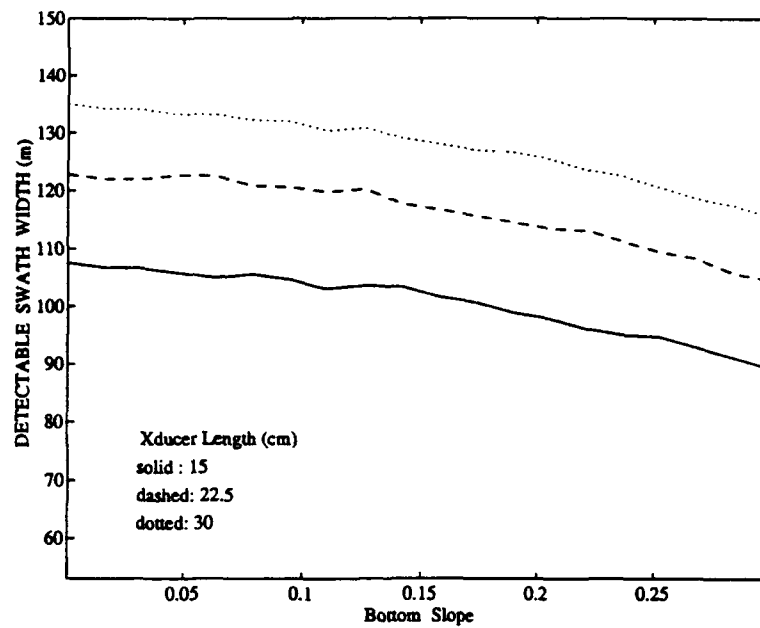


Figure 37 Detectable bottom swath width (DBSW) as a function of bottom slope and transducer length.

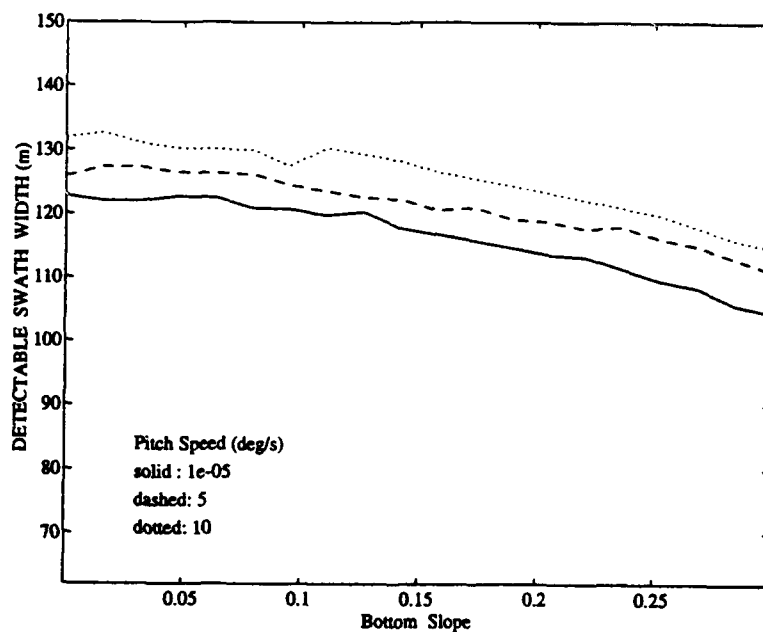


Figure 38 Detectable bottom swath width (DBSW) as a function of bottom slope and pitch rate.

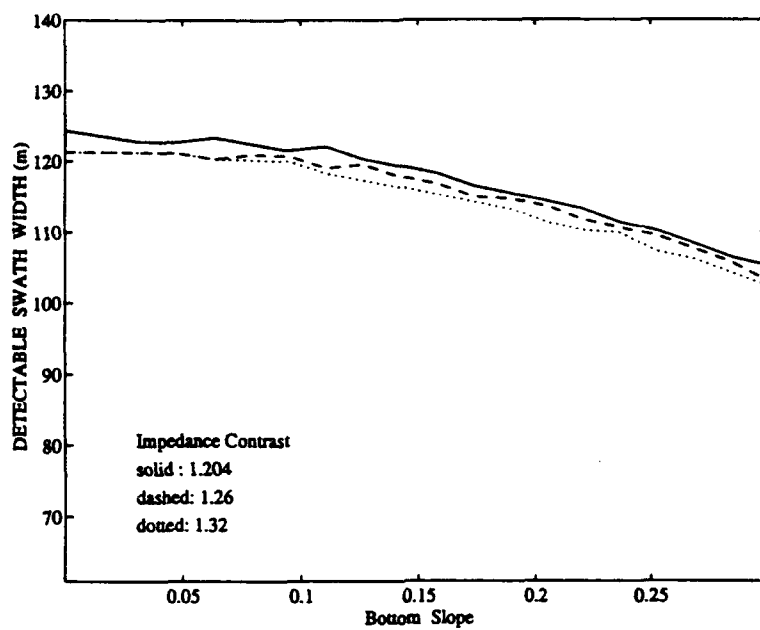


Figure 39 Detectable bottom swath width (DBSW) as a function of bottom slope and sediment-water impedance contrast.

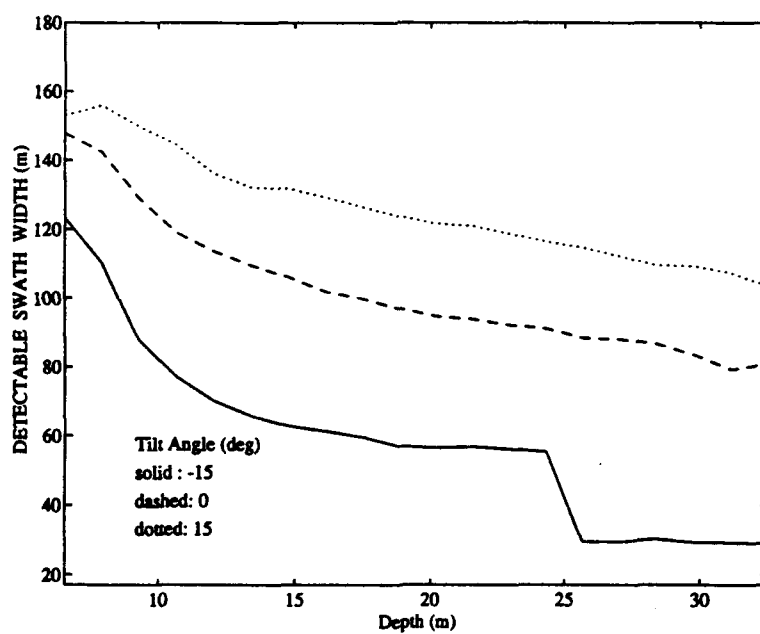


Figure 40 Detectable bottom swath width (DBSW) as a function of depth and transducer tilt angle.

5.3 Summary of Sensitivity Analysis

To conclude our sensitivity studies and to offer a more intuitive overview of the above discussions on the dependency (sensitivity) of DBSW on the different variables, Table 2 summarizes the results. Variables from left to right (symmetric to those from top to bottom) are arranged according to their relative influences on DBSW. In other words, transducer depth causes DBSW to increase the most while bottom depth causes DBSW to increase the least (decrease the most).

The value of subscript of I (increase) or D (decrease) reflects the degree of the change in DBSW, defined as:

0: $0 < \delta_{sw} \leq 10$ (m)

1: $10 < \delta_{sw} \leq 20$ (m)

2: $\delta_{sw} > 20$ (m)

where δ_{sw} represents the change in DBSW. Mixed behavior (denoted by M) means there was no apparent or consistent increasing or decreasing trend. In each rectangle in the table, there are two values; the one above the diagonal dashed line describes the dependence of DBSW on the variable in the same column (variable 1) while the one below the diagonal describes the dependence of DBSW on the variable in the same row (variable 2). We note here that the decision of whether DBSW is an increase (denoted by I) or a decrease (denoted by D) in Table 2 is based on a visual average over the three curves in each plot. It is, thus, a qualitative measure of how DBSW changes in terms of different variables.

TABLE 2. Performance Sensitivity

Var Var 2	Xducer Depth (Hx)	Tilt Angle (θ_i)	Xducer Width (Iz)	Xducer Length (Ix)	Pitch Speed (Vp)	Impedance contrast (Z)	Yaw Speed (Vy)	Bottom Slope (Ks)	Bottom Depth (H)
Xducer Depth (Hx)		I ₂	I ₂	I ₁	I ₀	M	D ₀	D ₁	
Tilt Angle (θ_i)	I ₂		M	I ₁	I ₀	D ₀	D ₀	D ₁	D ₂
Xducer Width (Iz)	I ₂	M		I ₁	I ₀	D ₀	D ₀	D ₂	D ₂
Xducer Length (Ix)	I ₂	I ₂	I ₂		I ₀	D ₀	D ₀	D ₁	D ₂
Pitch Speed (Vp)	I ₀	I ₂	I ₂	I ₂		D ₀		D ₁	D ₂
Impedance contrast (Z)	M	I ₂	D ₀	D ₀	I ₀		D ₀	D ₁	D ₂
Yaw Speed (Vy)	D ₀	I ₂	D ₁	D ₀		D ₁		D ₁	D ₂
Bottom Slope (Ks)	D ₁	I ₂	D ₂	D ₁	I ₀	D ₁	D ₁		D ₂
Bottom Depth (H)		D ₂	D ₂	D ₂	D ₂	D ₂	D ₂	D ₁	

I: Increase in DBSW

D: Decrease in DBSW

M: Mixed behavior (no
apparent increasing
or decreasing trend)

6.0 CONCLUSIONS

In this study, we have investigated the overall sonar performance in terms of the detectability of a target. We have included the effects of: (a) vehicle motion resulting in a motion loss in most cases; and (b) reverberation in a shallow water waveguide with small roughness boundaries and a penetrable bottom. Although the model is only approximate, the results qualitatively provide us with parameters for defining sonar performance under different circumstances.

In general, DBSW has stronger dependence on the geometric configuration of the sonar system, such as transducer position and tilt angle, than on such a physical properties of the environment as acoustic impedance. In another words, it is possible to optimize the system configuration to obtain the best sonar performance.

It is surprising that although vehicle motion can greatly affect the echo level, in most cases DBSW is relatively insensitive to vehicle motion and the results should be tested whenever possible. The weak dependence of DBSW on bottom acoustic impedance contrast is also quite surprising.

It is worth pointing out that since we used a simple quantity, DBSW, as a standard in evaluating sonar performance and because of the discontinuities in DBSW observed in many plots, DBSW may not reflect the true detectable volume of interest in some circumstances.

REFERENCES

- [1] Stewart, W. K., Multisensor Modeling Underwater with Uncertain Information, Ph.D. Thesis, Massachusetts Institute of Technology and Woods Hole Oceanographic Institution Joint Program, 1988.
- [2] Cobra, D. T., Geometric Distortions in Sidescan Sonar Images: A Procedure for Their Estimation and Correction, Ph.D. Thesis, Massachusetts Institute of Technology and Woods Hole Oceanographic Institution Joint Program, 1990.
- [3] Russell-Cargill, W. G. A., editor, *Recent Developments in Sidescan Sonar Techniques*, Central Acoustics Laboratory, University of Cape Town, South Africa, 1982.
- [4] Urick, R. J., *Principles of Underwater Sound*, McGraw-Hill, New York, 1983.
- [5] Jackson, D. R., A.M. Baird, J. J. Crisp, and P. A. G. Thomson, "High-frequency Bottom Backscatter Measurements in Shallow Water," *J. Acoust. Soc. Am.*, 80:1188-1199, 1986.
- [6] Mourad, P. D., and D. R. Jackson, "High-frequency Sonar Equation Models from Bottom Backscattering and Forward Loss," in *Proc. Oceans 89*, 1168-1175, 1989.
- [7] Dyer, I., Underwater Acoustics, unpublished, 1991.
- [8] Jin, G. and Z. Renhe, "Numerical Simulation of Average Reverberation Intensity In Shallow Water," *Acta Acoustica*, 15:252-257, (in Chinese), 1990.
- [9] Stanton, T. K., "Simple Approximate Formulas for Backscattering of Sound by Spherical and Elongated Objects," *J. Acoust. Soc. Am.*, 86:1499-1510, 1989.
- [10] Stanton, T. K., D. Chu, P. H. Wiebe, and C. S. Clay, "Average Echoes from Randomly-oriented Random-length Finite Cylinders: Zooplankton Models," (in press), *J. Acoust. Soc. Am.*, 1993.
- [11] Faran, J. J. Jr., "Sound Scattering by Solid Cylinders and Spheres," *J. Acoust. Soc. Am.*, 23:405-418, 1951.
- [12] Silbiger, A., "Scattering of Sound by an Elastic Prolate Spheroid," *J. Acoust. Soc. Am.*, 35:564-570, 1963.
- [13] Marston, P. L., "Geometrical and Catastrophe Optics Methods in Scattering," in "High-Frequency and Pulsed Scattering," *Physical Acoustics*, Vol. 21 (A. D. Pierce and R. N. Thurston, eds.) Academic Press, 1992.
- [14] Skudrzyk, E., *The Foundations of Acoustics*, Springer-Verlag, New York, 1971.

DOCUMENT LIBRARY

Distribution List for Technical Report Exchange - July 1, 1993

University of California, San Diego
SIO Library 0175C (TRC)
9500 Gilman Drive
La Jolla, CA 92093-0175

Hancock Library of Biology & Oceanography
Alan Hancock Laboratory
University of Southern California
University Park
Los Angeles, CA 90089-0371

Gifts & Exchanges
Library
Bedford Institute of Oceanography
P.O. Box 1006
Dartmouth, NS, B2Y 4A2, CANADA

Office of the International Ice Patrol
c/o Coast Guard R & D Center
Avery Point
Groton, CT 06340

NOAA/EDIS Miami Library Center
4301 Rickenbacker Causeway
Miami, FL 33149

Library
Skidaway Institute of Oceanography
P.O. Box 13687
Savannah, GA 31416

Institute of Geophysics
University of Hawaii
Library Room 252
2525 Correa Road
Honolulu, HI 96822

Marine Resources Information Center
Building E38-320
MIT
Cambridge, MA 02139

Library
Lamont-Doherty Geological Observatory
Columbia University
Palisades, NY 10964

Library
Serials Department
Oregon State University
Corvallis, OR 97331

Pell Marine Science Library
University of Rhode Island
Narragansett Bay Campus
Narragansett, RI 02882

Working Collection
Texas A&M University
Dept. of Oceanography
College Station, TX 77843

Fisheries-Oceanography Library
151 Oceanography Teaching Bldg.
University of Washington
Seattle, WA 98195

Library
R.S.M.A.S.
University of Miami
4600 Rickenbacker Causeway
Miami, FL 33149

Maury Oceanographic Library
Naval Oceanographic Office
Stennis Space Center
NSTL, MS 39522-5001

Library
Institute of Ocean Sciences
P.O. Box 6000
Sidney, B.C. V8L 4B2
CANADA

Library
Institute of Oceanographic Sciences
Deacon Laboratory
Wormley, Godalming
Surrey GU8 5UB
UNITED KINGDOM

The Librarian
CSIRO Marine Laboratories
G.P.O. Box 1538
Hobart, Tasmania
AUSTRALIA 7001

Library
Proudman Oceanographic Laboratory
Bidston Observatory
Birkenhead
Merseyside L43 7 RA
UNITED KINGDOM

IFREMER
Centre de Brest
Service Documentation - Publications
BP 70 29280 PLOUZANE
FRANCE

REPORT DOCUMENTATION PAGE	1. REPORT NO. WHOI-93-41	2.	3. Recipient's Accession No.
4. Title and Subtitle A Preliminary Study of Shallow-Water Sonar Issues: Signal Motion Loss and Reverberation Noise			5. Report Date September 1993
7. Author(s) W. Kenneth Stewart, Dezhang Chu, and Xiaou Tang			6.
9. Performing Organization Name and Address Woods Hole Oceanographic Institution Woods Hole, Massachusetts 02543			8. Performing Organization Rept. No. WHOI-93-41
			10. Project/Task/Work Unit No.
			11. Contract(C) or Grant(G) No. (C) N00014-92-C-6028 (G)
12. Sponsoring Organization Name and Address Office of Naval Research			13. Type of Report & Period Covered Technical Report
			14.
15. Supplementary Notes This report should be cited as: Woods Hole Oceanog. Inst. Tech. Rept., WHOI-93-41.			
16. Abstract (Limit: 200 words) This preliminary investigation addresses key program elements for sonar sensing in a shallow-water environment to establish bounds on possible solutions and to reduce program uncertainty. The modeling and experimental program focuses on two issues—the potential degradation of sonar data due to signal masking by shallow-water reverberation and signal loss caused by extreme platform motions. The research program combines theoretical analysis, experimental validation in a shallow-water environment, and development of a computer model to explore parametric sensitivity. Results from an initial dock-side test show good agreement with the theoretical predictions. From the shallow-water experiments and acoustic modeling we conclude that: (1) Signal motion loss can influence the reverberation level significantly but is not the dominant factor in target detection for sonars in the frequency range of interest (>200 kHz); a high-quality (velocity-aided) inertial navigation and attitude system will be sufficient to correct for geometric distortions caused by platform motion. (2) Although surface reverberation and multipath noise can be a factor, particularly in shadow-mode imaging, reverberation levels are rapidly attenuated at the frequencies of interest and beam patterns can be manipulated to reject most interferences; echo-mode imaging is still dominated by the contrast between target strength and bottom reverberation.			
17. Document Analysis			
a. Descriptors shallow-water acoustics target detection sonar modeling			
b. Identifiers/Open-Ended Terms			
c. COSATI Field/Group			
18. Availability Statement Approved for public release; distribution unlimited.	19. Security Class (This Report) UNCLASSIFIED		21. No. of Pages 55
	20. Security Class (This Page)		22. Price